Journal of Marine Research, 56, 937–993, 1998

Journal of MARINE RESEARCH

Volume 56, Number 5

On the stability of the wind-driven circulation

by P. Berloff[1] and S. P. Meacham[2,3]

ABSTRACT

This work examines the instabilities of steady circulations driven by stationary single-gyre wind forcing in closed rectangular basins with different aspect ratios. The stratified ocean is modeled with quasi-geostrophic 1.5-layer (equivalent-barotropic) and two-layer models. As friction is reduced, a stability threshold is encountered. In the vicinity of this threshold, unstable steady states and their unstable eigenmodes are determined. The structures of the eigenmodes and their associated energy conversion terms allow us to characterize the instabilities. In each case, the loss of stability is associated with an oscillatory instability. Several different instability mechanisms are observed. Which of these is responsible for the onset of instability depends upon the basin aspect ratio and the choice of stratification (1.5- or two-layer). The various mechanisms include instability of the western boundary current, baroclinic instability of the main recirculation gyre, instability of a standing meander located downstream of the main recirculation gyre and a complex instability involving several recirculations and the standing meander. The periods of the eigenmodes range from several months to several years depending upon the kind of instability and type of model. Additional insight into the western boundary current and baroclinic gyre instabilities is provided by an exploration of the stability of (a) the Munk boundary layer flow in 1.5- and two-layer models in an unbounded north-south channel, and (b) an isolated baroclinic vortex on an f-plane.

1. Introduction

The widespread use of ocean general circulation models (OGCMs) to simulate flows in realistic ocean basins, both in ocean only studies and in climate studies, obscures the fact

---

[1] Institute of Geophysics and Planetary Physics, University of California, Los Angeles, California, 90095, U.S.A.

[2] Department of Oceanography, Florida State University, Tallahassee, Florida, 32306, U.S.A.

[3] Present address: Department of Earth, Atmospheric and Planetary Sciences, MIT, Cambridge, Massachusetts, 02139, U.S.A.

that our understanding of the ocean's general circulation, and in particular its variability, is still rudimentary. This is exemplified by the continuing search for the origins of low-frequency variability in the ocean and in the climate system. From direct observations, it is known that there is considerable oceanic and atmospheric variability at decadal time scales. Several potential sources of such variability have been identified, including: oscillations of the thermohaline overturning circulation (e.g. Stommel, 1961; Nakamura *et al.,* 1994; Santer *et al.,* 1995), the response of the ocean to forcing containing an essentially stochastic component associated with synoptic variability in the atmosphere (e.g., Hasselmann, 1976; Wunsch, 1992; Frankignoul, 1995; Santer *et al.,* 1995), large-scale tightly coupled modes of the atmosphere-ocean system mediated by fluctuations in heat transport and surface heat fluxes induced by changes in the large-scale ocean gyres (e.g. Namias, 1959; Bjerknes, 1964; Namias, 1969; Latif and Barnett, 1994 and 1996; Goodman and Marshall, 1998), and eddy/mean flow interaction in the ocean (e.g. Bjerknes, 1964; Bryan, 1969; Holland and Lin, 1975a,b; Holland, 1978; Cox, 1987; Moro, 1990; Spall, 1996; Meacham, 1998a,b; Berloff and McWilliams, 1998). The latter process is driven by mesoscale instabilities with short time scales.

The manner in which mesoscale eddies produce low-frequency variability can be viewed from at least two perspectives. Synoptic eddies are the ocean analogue of weather and as such they can be regarded as forcing the slowly evolving baroclinic adjustment of the large-scale inertial recirculation gyres with "stochastic" mesoscale eddies producing low-frequency changes when "integrated" by the more slowly responding large-scale flow, c.f. Hasselmann (1976). This point of view downplays the spatially variable nature of the mesoscale eddy field. An alternative paradigm is the idea of eddy/mean flow interaction in which eddy potential vorticity fluxes and their divergence drive changes in the structure of the mean flow which in turn modifies the properties of the eddies. Such interactions are known to be capable of leading to low-frequency oscillations (e.g., Pedlosky, 1970).

Given the significant role that synoptic scale eddies play in the transport of properties within, and the variability of, the general circulation, it is important to understand their origin. A substantial body of theory deals with the basic mechanisms responsible for mesoscale variability in the ocean—barotropic, baroclinic and mixed instabilities—but almost all of it is in the context of either rectilinear flows, flows with a very slow spatial modulation, or axisymmetric flows. It is difficult to apply such theory directly to the large-scale ocean circulation in mid-latitudes because the flows there that are thought to be unstable are extremely asymmetric. Approximately straight currents are straight only for distances two or three times larger than the wavelength of the most unstable mode predicted by rectilinear stability theory. Here, we investigate the stability properties of some of the asymmetric steady state circulations that exist in idealized models of the general circulation.

We explore the linear stability of the wind-driven quasi-geostrophic circulation in a rectangular closed basin. We consider two models of a stratified flow. The first model has only one active layer of fluid on top of an infinitely deep motionless layer, the single-layer, reduced-gravity, quasi-geostrophic model, or, more concisely, the equivalent-barotropic model (EB hereafter). The second model is a two-layer, quasi-geostrophic model (2LQG). Because of the presence of an active second layer, the latter model allows the possibility of baroclinic instability, a process excluded in the EB model.

The steady states and the nonlinear time-dependent behavior of the steadily forced EB and 2LQG models were studied in Berloff and Meacham (1997) (hereafter BM1) and Berloff and Meacham (1998) (hereafter BM2), respectively. Here we look more closely at the origin of time dependence in these models and focus on the behavior of the linear instabilities of some of those steady states and their dependence on basin aspect ratio. In both models the steady circulations contain robust features such as a western boundary current and several inertial recirculation gyres. In principle, both the gyres and the current could be potential sites of instability. In addition, a global mode of the quiescent basin (a basin mode) may be destabilized by the presence of the stationary circulation. One of our goals is to find out whether one can identify localized regions that drive instabilities of the basin-wide circulation. To assist in this task, we supplement the numerical stability study of the full circulation, which is strongly asymmetric, by analyzing the stability of several symmetric problems: equivalent-barotropic and two-layer quasi-geostrophic western boundary currents and vortices in greatly simplified process models. Locally rectilinear or approximately circular flows occur as features of the steady circulations seen in the full basin. The critical Reynolds numbers, Re_c, and the structures of the most unstable eigenmodes found in these simplified problems are compared with the critical Re_c and the most unstable eigenmodes of the full circulation found at the onset of instability.

In the first subsection of the introduction, we briefly review some relevant work concerning the stability of vortices on an f-plane and jets on a β-plane. In the second subsection, we discuss the literature dealing with instabilities of steady-state circulations found in general circulation models (GCMs).

a. *Linear stability of jets and vortices*

The study of the stability of parallel shear flows on a β-plane was pioneered by the works of Howard and Drazin (1964) and Dickinson and Clare (1973). They showed that, in the long-wave approximation, the hyperbolic-tangent shear flow has two sets of unstable modes when β is nonzero. One set is like the instability of a vortex sheet (this set merges with the zero β unstable mode), and the other set is essentially Rossby-wavelike on the side of the shear zone where the flow is westerly (this set vanishes for sufficiently small β).

The instability of barotropic zonal jets was studied by Talley (1983a). It was shown that there are again two classes of linearly unstable modes. The modes of the first type are trapped to the jet and have larger growth rates. The modes of the second type have small growth rates and take the form of "radiating modes." The latter are only weakly trapped to the current, having a Rossby wavelike appearance in the far field with only a slow decay in the cross-stream direction. Talley went on to consider baroclinic two-layer quasi-geostrophic jets (Talley, 1983b) and showed that one can again distinguish between strongly trapped and radiating instabilities. She observed that purely westward jets had radiating instabilities with growth rates comparable to those of trapped instabilities. All unstable modes of purely eastward jets were trapped. One of the distinctions between the different types of instabilities that we will see below is the degree to which they radiate energy from the region in which the instability is exchanging energy with the basic flow.

Viscously damped shear instability in barotropic western boundary currents, advanced as a mechanism for introducing time dependence to the general circulation by Bryan (1963) amongst others, was studied by Ierley and Young (1991) (hereafter IY). The western boundary current in that study was modeled by an idealized parallel flow in an unbounded meridional channel. The critical Reynolds number at which the flow became unstable was found to be between 20 and 100 depending upon the details of the velocity profile. IY found that the most unstable modes are trapped at the western boundary. The trapped modes had slowly decaying oscillatory tails as one moved eastward. The Rossby wave channel modes that are the channel analogues of radiating instabilities were found to be more stable than the trapped modes in the sense that they did not grow until the Reynolds number was considerably higher.

Flierl (1988) studied the instability of inviscid barotropic and baroclinic quasi-geostrophic vortices on an *f*-plane. The vortices were modeled by a circular region of horizontally uniform potential vorticity surrounded by an annulus of uniform but different potential vorticity. The vortices were isolated, i.e. they had no circulation in the basic state outside the outer radius. The results showed that three types of instability exist for isolated vortices:

(i) Purely barotropic instability may occur when the outer annulus is narrow enough. This situation corresponds to strong shear at the outer edge of the eddy. In that case the second azimuthal mode ($m = 2$) becomes unstable first. This instability leads to a break-up of the vortex into either dipoles or tripolar states.

(ii) If the eddy contains enough baroclinic flow, has a large scale compared to the deformation radius and if the outer shear occupies a broad region, then it is baroclinically unstable with the most unstable mode being the second azimuthal mode. The stability of the vortex then depends upon the amount of barotropic flow in the vortex. This instability leads to nonlinear vacillations of the vortex (Helfrich and Send, 1988).

(iii) For baroclinic vortices with sizes smaller than the deformation radius, a "twisting" instability may exist, as found initially by Gent and McWilliams (1986). This instability occurs when the deep flow co-rotates with the surface flow. This instability involves a tilting of the vortex axis and a horizontal separation between the deep vortex and the surface vortex.

b. Instabilities found in GCMs

The existence of a critical Reynolds number, Re_c, for a barotropic circulation driven with single-gyre wind forcing and damped by lateral friction was shown by Bryan (1963). The boundary conditions in that case were no-slip on the meridional walls and free-slip on the zonal walls. Bryan found that if $Re < Re_c$, then, during the adjustment process, transient oscillations associated with the initial spin-up decayed and, at large times, the circulation reached a steady state. For supercritical Re, steady states were never achieved, and the flow oscillated, seemingly irregularly, around some mean state. The oscillations were associated with a train of disturbances moving along the western boundary. Bryan hypothesized that the origin of the oscillations was shear-flow instability in the western boundary current.

The barotropic circulation driven by a double-gyre wind forcing and damped by bottom and biharmonic friction was studied by LeProvost and Verron (1987). In that case the boundary conditions were free-slip. Both steady and time-dependent solutions were identified in parameter space. The time-dependent circulation contained two major types of disturbances. One type was associated with the meandering of the eastward jet, and the other with radiation of Rossby wavelike features from the westward return flow.

Moro (1990) found Re_c for the steady states of the barotropic circulation driven by an asymmetric double-gyre wind stress. The problem included lateral friction and no bottom friction. Moro studied the effects of both no-slip and free-slip boundary conditions. He showed that the onset of instability was associated with a supercritical Hopf bifurcation (Drazin, 1992), i.e. an oscillatory instability that gave rise to stable periodic flows for $Re > Re_c$, with oscillation amplitudes that approach zero like $(Re - Re_c)^{1/2}$. The steady solutions, unstable for $Re > Re_c$, contained not an eastward jet, but rather a large-scale vortex street, connecting the western intensifications with the regions of slow return flow. The oscillations were associated with vortex shedding from the entire vortex street.

Sheremet *et al.* (1997) studied the linear stability of a barotropic single-gyre circulation with no-slip conditions at the meridional walls and free-slip conditions at the latitudinal walls. They found several modes of instability. As Re was increased, a mode trapped at the western wall became unstable first. A mode associated with disturbances in the recirculation gyre started to grow at larger Re. This second mode was associated with a stronger signal in the eastern half of the basin than the first mode. These results were in good agreement with the numerical experiments of Kamenkovich *et al.* (1995) and Sheremet *et al.* (1995), who also showed that the onset of instability with increasing Re was associated with the growth of an eigenmode trapped to the western wall. For a slightly supercritical Re, the growing disturbance saturated, producing a limit cycle. The amplitude of the nonlinear oscillations on the limit cycle increased with increasing supercriticality. All these facts helped to characterize the onset of instability as a Hopf bifurcation of the flow.

The double-gyre 1.5-layer shallow-water model with both free-slip and no-slip boundary conditions on the walls was studied by Jiang *et al.* (1995) and Speich *et al.* (1995). In that case, the instability of the steady state was associated with a Hopf bifurcation. However, they concluded that the western boundary layer was not the source of the instability, instead supercritical limit cycle oscillations were related to the appearance of multipole vortices across the eastward jet.[4]

[4] A study of the instabilities of the steady solutions of a double-gyre two-layer quasi-geostrophic model has recently been published by Dijkstra and Katsman (1997).

The stability analysis of a barotropic single-gyre circulation in a relatively small basin with no-slip boundary conditions was described in Meacham and Berloff (1997a; hereafter MB1) and Meacham and Berloff (1997b; hereafter MB2). It was shown that the instability can be of two types. One was an instability of the western boundary layer, similar to the instability examined by Ierley and Young (1991) for the case of the western boundary current in an unbounded north-south channel (class A, say). The other instability (class B) was associated with growing disturbances in the meander located to the east of the main recirculation gyre. Both types of instability were oscillatory. Several different modes of class B instability were observed; these were differentiated by the zonal scale of the Rossby wavelike tail in the eastern half of the basin. It was shown that the Hopf bifurcation may be either supercritical or subcritical (Drazin, 1992) in the circulation regimes explored, depending on the basin geometry and the strength of the wind-stress. Meacham and Berloff (1997b) observed resonances between the class B instabilities of the steady circulation and the normal modes of the basin.

Some properties of the instabilities of the EB circulation in the case of single-gyre wind forcing, no-slip boundary conditions and a fixed basin size ($L_x = 800$ km, $L_y = 400$ km) were apparent in the nonlinear study of BM1. There, the most unstable eigenfunction was trapped in the western part of the basin, but the instability could not be characterized as an instability of the western boundary layer, or the meander, or the main recirculation gyre separately. The energy exchange between the eigenmode and the mean flow involved the western boundary intensification, western recirculation and the meander between the southwestern and the central gyres. This complex instability was associated with a supercritical Hopf bifurcation of the flow. The 2LQG circulation in the same basin with single-gyre wind forcing and no-slip boundary conditions was the focus of the bifurcation study in BM2. Although a supercritical Hopf bifurcation was observed there too, the circulation was less stable and the character of the instability was different to that seen in the EB model. The growing disturbances in BM2 were triggered by baroclinic instability in the southwestern recirculation gyre.

Unlike BM1 and BM2, this paper deals with the linear instabilities of steady circulations. It examines their dependence on such factors as deformation radius and basin size, as well as comparing the structure of the unstable modes with instabilities of simple jets and vortices.

This work differs from Sheremet *et al.* (1997) and MB2 in that we use models of stratified flows rather than a homogeneous layer. Unlike Jiang *et al.* (1995), the problem we consider includes wind stress forcing with a curl of single sign which may be a better approximation for small basins like the Black Sea, as opposed to the double-gyre forcing used in models of larger mid-latitude basins.

c. *Plan of the paper*

The plan of the paper is as follows. In Section 2, we briefly describe the models of the wind-driven circulation which we use in Sections 3 and 4 to study the primary instability of

Table 1. Dimensional parameters of the models.

H_1	upper layer depth
H_2	lower layer depth in two-layer model
$\tau_0 = 0.05\ \mathrm{Nm}^{-2}$	wind stress amplitude
$f_0 = 0.93 \times 10^{-4}\ \mathrm{s}^{-1}$	Coriolis parameter
$\beta_0 = 2 \times 10^{-11}\ \mathrm{m}^{-1}\ \mathrm{s}^{-1}$	planetary vorticity gradient
$R_d = \dfrac{\sqrt{g' H_1}}{f_0} = 24.40\ \mathrm{km}$	deformation radius in the equivalent-barotropic model
$R_d = \dfrac{\sqrt{g'}}{f_0}\sqrt{\dfrac{H_1 H_2}{H_1 + H_2}} = 23.15\ \mathrm{km}$	deformation radius in the two-layer model
$\Delta x = \Delta y = 6.25\ \mathrm{km}$	grid spacing

the wind-driven circulation in rectangular basins. In Section 5, we explore the stability of the western boundary current in the EB and 2LQG models with lateral friction by looking at model boundary currents in an unbounded meridional channel. This extends the barotropic study of IY and, in the case of the 2LQG model, permits baroclinic and mixed instabilities in addition to barotropic instabilities. The boundary conditions imposed on the flow at the lateral walls are no-slip and no-flow through the boundaries. A discussion comparing the boundary current instabilities with some of the instabilities seen in Sections 3 and 4 is included in Section 5. In Section 6, we study the stability of isolated circular vortices in the 2LQG model with lateral friction. Each vortex is centered in a circular basin with a radius much larger than the characteristic radius of the vortex. The boundary conditions are the same as in Section 5. In Section 7, we briefly summarize the results from the previous sections.

2. Numerical circulation models

The nonlinear dynamics of the numerical models which we use were explored in BM1 and BM2 for a wide range of viscosity coefficients but a fixed basin aspect ratio. We study the primary linear instability of the wind-driven circulation in basins with different aspect ratios. We define the primary instability as the instability that occurs first when the Reynolds number of the flow is increased. The dimensional parameters of the models are listed in Table 1. In the case of the EB model, the depth of the lower layer, H_2, $\rightarrow \infty$, and the internal deformation radius, R_d, $\rightarrow$ $\sqrt{g' H_1}/f_0$. In the two-layer case, $R_d = (\sqrt{g'}/f_0)\sqrt{H_1 H_2/(H_1 + H_2)}$. The wind stress has a uniform curl of τ_0/L_x. In all experiments, τ_0 is fixed at 0.5 dyn/cm².

We use the Sverdrup balance in the upper layer to specify the velocity scale: $U = \tau_0(\rho H_1 L_x \beta_0)^{-1}$. The nondimensional parameters of the problem are

$$\delta = \frac{L_y}{L_x}; \quad \varepsilon = \left(\frac{\delta_I}{L_x}\right)^2; \quad \mu = \left(\frac{\delta_M}{L_x}\right)^3; \quad S = \left(\frac{L_x}{R_d}\right)^2; \quad \gamma = \frac{H_1}{H_2}, \tag{1}$$

where δ_I, $= (U/\beta_0)^{1/2}$, is an inertial boundary layer width scale and δ_M, $= (\nu/\beta_0)^{1/3}$, is the viscous (Munk) boundary layer width scale (Pedlosky, 1987). We define a Reynolds number for the problem by $Re = UL_x/\nu = \varepsilon/\mu$. The two-layer quasi-geostrophic potential vorticity equations are

$$\begin{aligned} \frac{\partial \zeta_1}{\partial t} + \varepsilon J(\psi_1, \zeta_1) + \frac{\partial \psi_1}{\partial x} &= \nabla \times \tau + \mu \nabla^4 \psi_1 \\ \frac{\partial \zeta_2}{\partial t} + \varepsilon J(\psi_2, \zeta_2) + \frac{\partial \psi_2}{\partial x} &= \mu \nabla^4 \psi_2, \end{aligned} \tag{2}$$

where the potential vorticities $\zeta_{1,2}$ corresponding to the upper and lower layers are

$$\begin{aligned} \zeta_1 &= \left(\nabla^2 - \frac{S}{1+\gamma}\right)\psi_1 + \frac{S}{1+\gamma}\psi_2 \\ \zeta_2 &= \left(\nabla^2 - \frac{S\gamma}{1+\gamma}\right)\psi_2 + \frac{S\gamma}{1+\gamma}\psi_1 . \end{aligned} \tag{3}$$

The boundary conditions are no-flow through the lateral boundaries and no-slip:

$$\psi_{1,2|C} = \Gamma_{1,2}(t), \qquad \left.\frac{\partial \psi_{1,2}}{\partial n}\right|_C = 0, \tag{4}$$

were C is the basin's bounding contour. The conservation of mass in each layer provides constraints on the integrated streamfunctions,

$$\frac{\partial}{\partial t} \iint_A \psi_i(x, y)\, dx\, dy = 0, \qquad i = 1, 2, \tag{5}$$

and hence determines $\Gamma_i(t)$. In the EB case ($H_2 \to \infty$), $\psi_2 \equiv 0$, $\gamma \equiv 0$ and the second equations from both (2) and (3), as well as the boundary conditions and mass conservation constraint for the lower layer, become irrelevant since the lower layer is assumed to be at rest. The governing potential vorticity equation becomes

$$\frac{\partial}{\partial t}\zeta_1 + \varepsilon J(\psi_1, \nabla^2\psi_1) + \frac{\partial \psi_1}{\partial x} = \nabla \times \tau + \mu \nabla^4 \psi_1, \tag{6}$$

where

$$\zeta_1 = (\nabla^2 - S)\psi_1 . \tag{7}$$

A brief description of the numerical implementation of (2)–(7) is given in Appendix A.

The steady states of both the EB problem and the 2LQG problems are identical to those of a homogeneous ocean with a depth equal to that of the upper layer in the stratified problems. The presence of lateral friction and no-slip boundary conditions in the lower layer, together with the absence of diabatic mass fluxes, means that when the upper layer is steady, the lower layer must come to rest. The upper layer steady state streamfunction then satisfies an equation with no information about R_d or the lower-layer depth:

$$\varepsilon J(\psi_1, \nabla^2\psi_1) + \frac{\partial\psi_1}{\partial x} = \nabla \times \tau + \mu\nabla^4\psi_1. \tag{8}$$

However, the stability properties of the steady states depend strongly on R_d and H_2 (Appendix A).

Ideally, one would wish to find the hypersurface in the 5-dimensional parameter space (ε, μ, S, δ, γ), that separates the stable steady solutions from the unstable ones but this is far too difficult to compute. We explore the primary instability of the circulation in basins with three different aspect ratios, $\delta = 2, 1, 0.25$. $L_x = 800$ km for $\delta = 2$ and 1 and $L_x = 1600$ km for $\delta = 0.25$ (we refer to the previous studies of BM1 and BM2 for a fourth aspect ratio, $\delta = 0.5$ and $L_x = 800$ km). As we vary δ, the pre-eminent instability mechanism changes. We fix all parameters except ν and then locate the instability threshold that is encountered as ν is varied (when ν is varied, μ is the only nondimensional parameter to change). We use the evolutionary model described in the previous paragraph to find the stability threshold using the procedure outlined in Appendix A. Once the threshold has been found, a value of ν is chosen close to the threshold value but on the unstable side of the threshold, so that only one normal mode is unstable and the imaginary part of its eigenfrequency is small compared to the real part. The unstable normal mode is then found using a procedure built around the evolutionary model. This, too, is described in Appendix A. Below, we first examine the spatial structure of the linear instabilities of the EB and 2LQG wind-driven circulation models. Later, we will compare these with some simpler stability problems in order to try and characterize the nature of the circulation instabilities. We analyze the spatio-temporal structure of the unstable eigenmodes and compute the eddy-mean energy conversion terms associated with their growth. The spatial structure of the conversion terms helps us to localize the most unstable parts of the flow and to characterize the instability.

All of the primary bifurcations of the flow that we found were supercritical Hopf bifurcations (to a local accuracy equal to the distance between the neighboring values of ν for which the experiments were performed). A subcritical Hopf bifurcation associated with one of two branches of stable time-dependent attractors of the wind-driven circulation was found in MB1 for the barotropic case. It is possible that additional branches of stable time-dependent attractors associated with subcritical bifurcations may also exist in the EB and 2LQG problems; however, here we limit our attention to the *primary* linear instabilities, the instabilities that occur at the lowest Reynolds numbers.

3. Primary instability of the wind-driven equivalent-barotropic circulation

In the present section, we address the question of whether the dominant instabilities of a steady circulation are associated with particular features of the circulation (inertial recirculations, western boundary current, main standing meander and westward return flow) and whether this association changes as the basin shape is varied. Some of the questions that we seek to answer are: How does the character of the instability change as the basin shape changes? Are the unstable modes trapped near strong circulation features? Do they radiate energy into the interior of the basin (c.f., Talley, 1983)? Below, we first describe the nature of the instabilities that are found, then we discuss the results.

An analysis of the way in which energy is extracted from the basic state by a growing eigenmode helps identify the mechanism responsible for an instability. The full energy density of an EB basic state is

$$E = \frac{|\nabla \Psi_1|^2}{2} + S\frac{\Psi_1^2}{2}, \tag{9}$$

where $\Psi_1(x, y)$ is the streamfunction of the unstable steady state. The slowly varying mean perturbation energy density of a small amplitude, slowly growing, normal mode of the EB flow is

$$\langle E' \rangle = \left\langle \frac{|\nabla \psi_1'|^2}{2} \right\rangle + S\left\langle \frac{\psi_1'^2}{2} \right\rangle, \tag{10}$$

where $\psi_1'(x, y, t)$ is the perturbation streamfunction associated with the growing unstable eigenmode and

$$\langle f(t) \rangle (t_0) \equiv \frac{1}{T}\int_{t_0}^{t_0+T} f(t)\, dt \tag{11}$$

represents time averaging over one period, T, of the slowly growing oscillatory eigenmode. This exploits the separation in time scale between the oscillation period and the e-folding time for an oscillatory instability close to the bifurcation threshold. The perturbation energy is a positive definite functional of ψ' so that if a perturbation is to grow, it must extract energy from the basic state. The energy equations of the EB model are derived in Appendix B.

For an EB flow, the energy exchange (Appendix B) between the basic state and the perturbations can be expressed in the form:

$$P = -\varepsilon \langle \psi_{1x}' J(\psi_1', \Psi_{1x}) + \psi_{1y}' J(\psi_1', \Psi_{1y}) \rangle. \tag{12}$$

When the area integral of P is positive, perturbations gain energy from the basic state and grow. P has a unique representation only up to the addition of a term that can be expressed as the divergence of a flux that vanishes on the boundaries of the domain. The area integral of any such addition is zero. Different forms of the conversion were compared in MB1 and BM1, and were found to give qualitatively similar results. We limit ourselves only to (12) and regard regions of strong positive values of P as sites that drive the instability. This is not a rigorous idea since we are dealing with normal modes of the whole basin-wide flow and, in principle, each part of the basin can have an effect on the phase of ψ_i' in every other

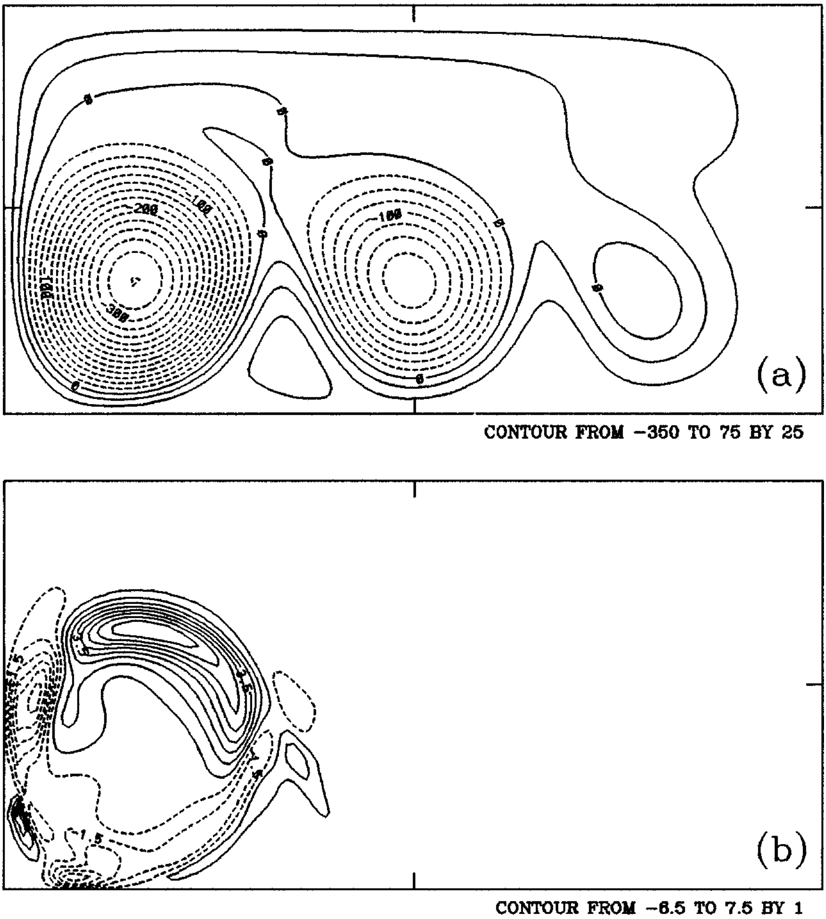

Figure 1. (a) The streamfunction of the unstable equivalent-barotropic steady state at $\nu = 102$ m^2/sec (CI = 30). $L_y = 0.5L_x = 400$ km. (b) The spatial distribution of the energy conversion term P for the most unstable eigenmode of the circulation shown in (a).

part of the basin. However, heuristically, the approach appears useful—the instabilities that we identify all have localized regions of strong energy conversion. An unstable steady state from BM1 (Fig. 1a) for a basin with $L_y = 0.5L_x = 400$ km and $\nu = 102$ m^2/sec is dominated by recirculation gyres and only a small part of the interior of the basin resembles a Sverdrup flow. The corresponding P (Fig. 1b), associated with the unstable normal mode, is concentrated in the northern part of the south-western gyre where there is a relatively strong westward flow.

Here we explore the structures of the most unstable eigenmodes and the energy conversions P associated with them in three basins with different sizes: $L_y = 2L_x = 1600$ km, $L_y = L_x = 800$ km, $L_y = 0.25L_x = 400$ km. The dimensional parameters (Table 1)

Table 2. Re_c, ν_c and T_c for the onset of instability in equivalent barotropic basins of size $L_x \times L_y$.

L_y (km)	L_x (km)	Re_c	ν_c ($m^2\ s^{-1}$)	T_c (days)
1600	800	79	158	687
800	800	75	166	549
400	800	120	104	112
400	1600	51	245	949

are the same as in BM1 and are motivated by the structure of the Black Sea. Note that the wind stress is cyclonic. Some of the critical values are summarized in Table 2.

a. Basin with $L_y = 2L_x = 1600$ km

In the basin with $L_y = 2L_x = 1600$ km, the onset of linear instability occurs at a critical value of ν, ν_c, located between 157 and 160 m²/sec ($Re_c \simeq 79$). The unstable steady state at $\nu = 155$ m²/sec (Fig. 2) has a well developed western boundary current, a northward

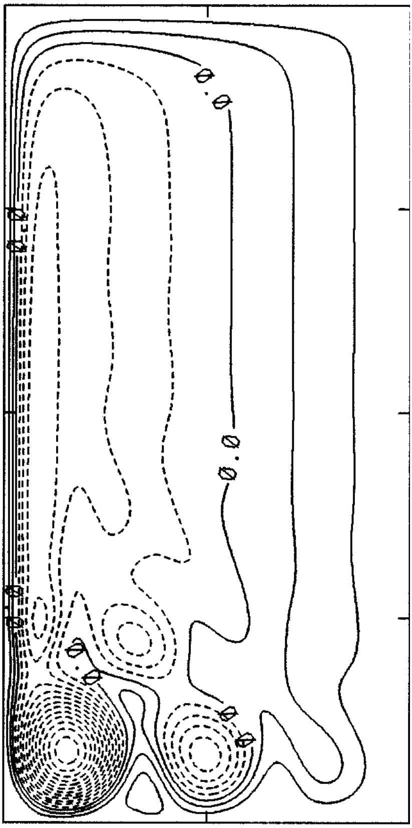

Figure 2. The streamfunction of the unstable equivalent-barotropic steady state at $\nu = 155$ m²/sec (CI = 30). $L_y = 2L_x = 1600$ km.

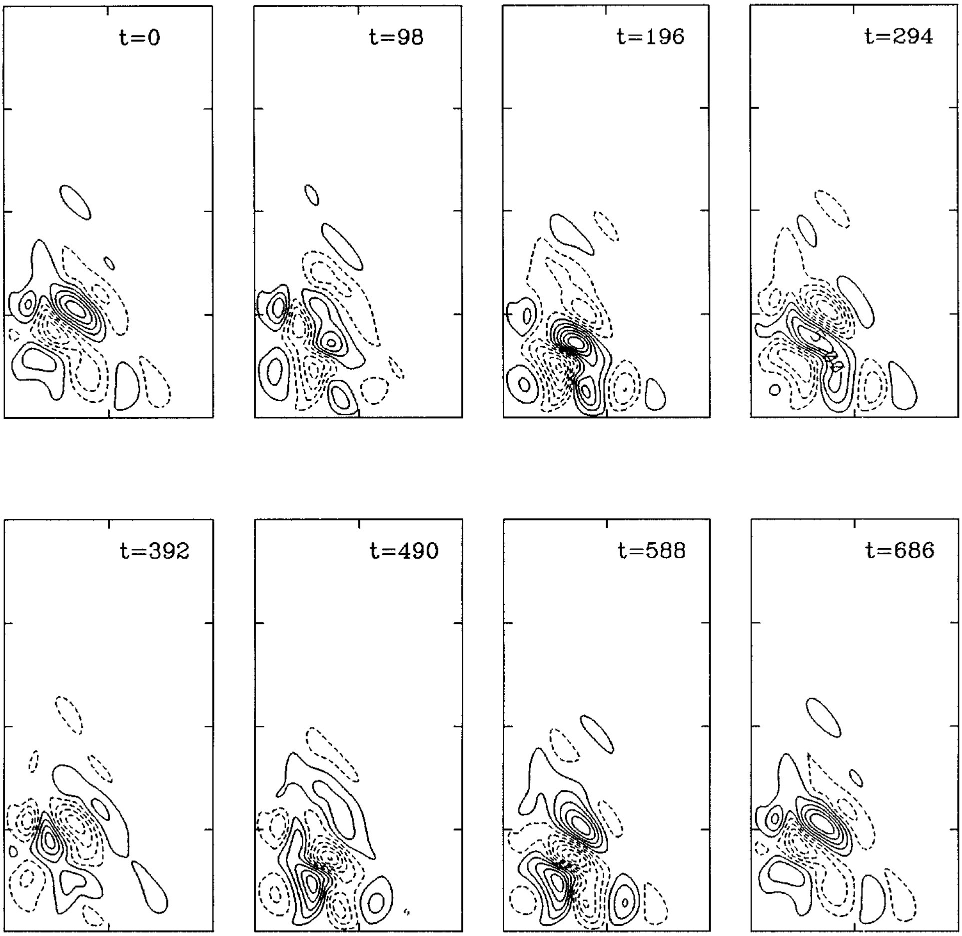

Figure 3. Time-dependent behavior of the streamfunction of the most unstable eigenmode at $\nu = 155\ \mathrm{m^2/sec}$ over one period. $L_y = 2L_x = 1600$ km. Time t is measured in days.

Sverdrup flow (a typical velocity is about 1.6 cm/sec) in the interior of the basin and five recirculation cells in the southern part of the basin. Subsequently, we will refer to these recirculations in the following way: the biggest one in the southwestern corner of the basin—the southwestern gyre; the one located to the east of the southwestern gyre—the central gyre; the one located to the north of the southwestern gyre—the western recirculation; the one located to the northeast of the southwestern gyre—the central recirculation, and the one located to the east of the central gyre—the eastern recirculation. In the western boundary current, the flow velocity is about 31 cm/sec at maximum and it reaches 39 cm/sec in the region where the current merges with the southwestern recirculation gyre.

The most unstable eigenmode at $\nu = 155\ \mathrm{m^2/sec}$ has a period of 687 days and a complicated structure (Fig. 3) consisting of several eddies located in the southern half of

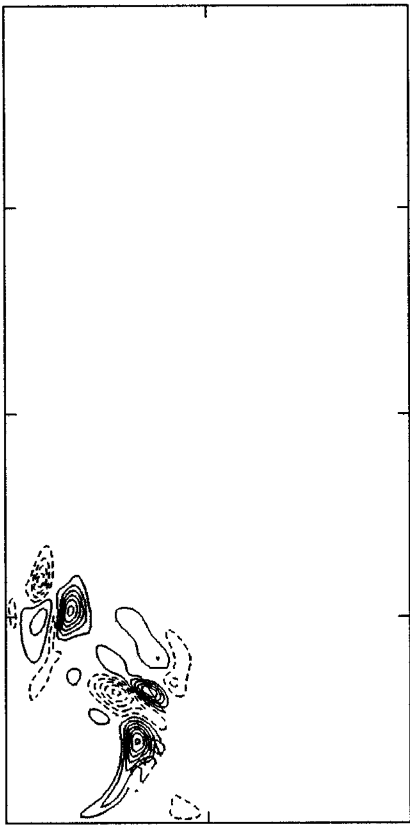

Figure 4. The spatial distribution of the energy conversion term P for the most rapidly growing eigenmode at $\nu = 155$ m^2/sec (CI $= 0.5 \times 10^{-6}$). $L_y = 2L_x = 1600$ km.

the basin and advected by the recirculations. In comparison, the eigenmodes of the baroclinic circulation (Section 4) are simpler and may be more readily identified with distinct features of the steady flow. The energy exchange P (Fig. 4) has one maximum that is associated with the western part of the meander between the southwestern and the central gyres; another maximum that is localized in the northern part of the same meander and the southern edge of the central recirculation; third and fourth maxima are associated with the weak western recirculation. The structure of P suggests that the instability involves 3 out of the 5 recirculations (without the weak eastern recirculation and the central gyre) and the meander between the southwestern and central gyres. It is interesting that the western boundary current is stable in this case. Both the instability in Figure 16 and that in Figures 3 and 4 are consistent with the idea that the enhanced stability of EB flows means that western boundary current instability is inhibited until rather high Re are reached. This allows the strong inertial recirculations to go unstable before the western boundary current.

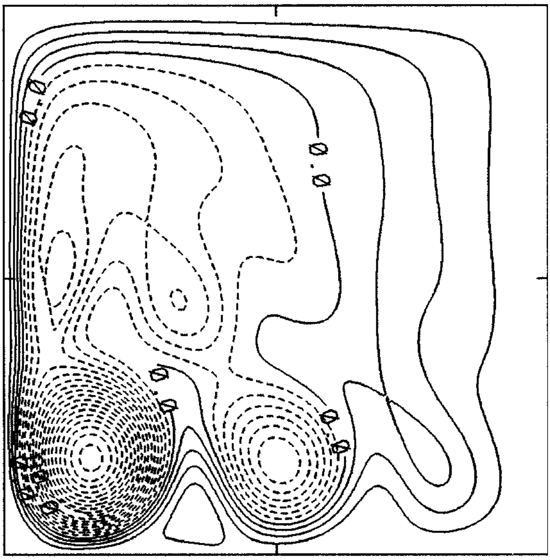

Figure 5. The streamfunction of the unstable equivalent-barotropic steady state at $\nu = 165$ m^2/sec (CI = 20). $L_y = L_x = 800$ km.

In the baroclinic case (Section 6) the western boundary current in the basin with $L_y = 2L_x = 1600$ km loses stability at a significantly smaller Re_c.

b. Basin with $L_y = L_x = 800$ km

In the basin with $L_y = L_x = 800$ km, the ν_c associated with the onset of oscillatory instability lies between 165 and 168 m^2/sec ($Re_c \simeq 75$), which means that the circulation is slightly less stable than in the basin with $L_y = 1600$ km. The period of the linear eigenmode growing on the unstable steady state (Fig. 5) at $\nu = 165$ m^2/sec is 549 days. The spatio-temporal structure of the eigenmode (not shown) is similar to that found with $L_y = 2L_x = 1600$ km. The spatial distribution (Fig. 6) of P computed for the eigenmode is similar to that in Figure 4, but the maxima associated with the meander have smaller amplitudes than the maxima located at the western recirculation, suggesting that as L_y is decreased, the main energy source of the instability shifts from the meander to the western recirculation.

In Section 6 it will be shown that in the baroclinic case the instability of the circulation in the basin with $L_y = L_x = 800$ km is due to a local baroclinic instability of the southwestern gyre. This type of instability was also found in BM2 for a basin with $L_y = 0.5L_x = 400$ km.

c. Basin with $L_y = 0.5L_x = 400$ km

The earlier study of BM1 considered a basin with $L_x = 800$ km and $L_y = 400$ km. The steady state near the onset of stability contained only three recirculations (Fig. 1a); the northern and central recirculations did not "fit" into the basin. A central recirculation was

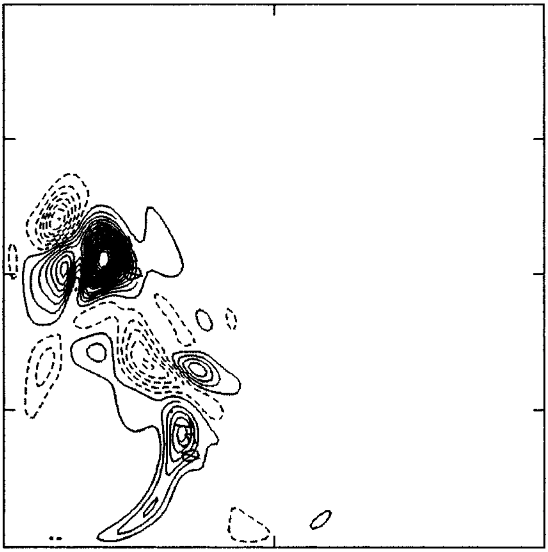

Figure 6. The spatial distribution of the energy conversion term P for the most rapidly growing eigenmode at $\nu = 165\ \mathrm{m^2/sec}$ ($\mathrm{CI} = 0.5 \times 10^{-6}$). $L_y = L_x = 800$ km.

observed in some of the instantaneous streamfunction fields from time-dependent solutions and in the fields obtained by time-averaging over the basic period of the quasi-periodic circulation observed at low viscosity. The period of the unstable eigenmode at the onset of instability was 112 days.

The dominant maximum of the energy conversion term, P, lay in the western part of the southwestern gyre, although a very small local maximum in the meander was also present. The fact that the main energy source is not in the meander but in the western part of the basin, is consistent with the trend seen on going from the $\delta = 2$ to $\delta = 1$. This change in character of the instability as one passes to the 800 km × 400 km basin results in a much more stable flow with a critical Reynolds number of 120.

d. Basin with $L_y = 0.25L_x = 400$ km

Lastly, we considered a basin with a relatively large zonal width, $L_x = 1600$ km, compared to its meridional size, $L_y = 400$ km. The amplitude of the wind stress, τ_0, remained unchanged, but its curl was reduced by a factor of two in order to keep the total Sverdup transport over the basin the same as in all other experiments. Because of the change in L_x, the nondimensional parameters change in the following way: $\delta \rightarrow \delta/2$, $\varepsilon \rightarrow \varepsilon/8$, $\mu \rightarrow \mu/8$ and $S \rightarrow 4S$. The significant reduction of ε leads to a less nonlinear flow for a given value of ν. However, the primary Hopf bifurcation occurs at ν_c between 240 and 250 $\mathrm{m^2/sec}$ ($Re_c \simeq 51$), a lower value of Re_c than was the case for the $\delta = 2, 1, 0.5$ basins; this example is the least stable. The unstable steady state at $\nu = 240\ \mathrm{m^2/sec}$ (Fig. 7) has three cyclonic recirculations of unequal strength, a westward jet in the northwestern part of the basin and a meandering eastward jet in its southwestern part. The velocity reaches

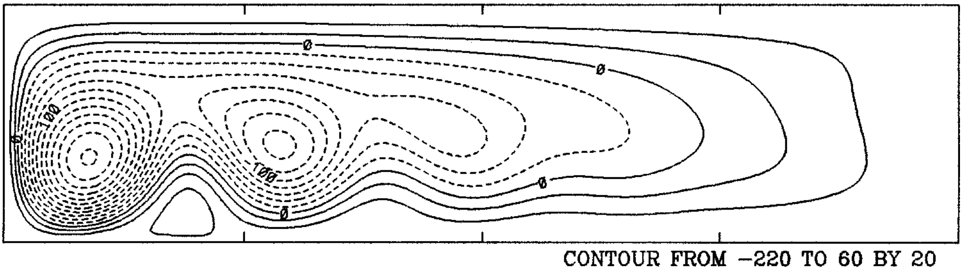

Figure 7. The streamfunction of the unstable equivalent-barotropic steady state at $\nu = 240\ \mathrm{m^2/sec}$ (CI = 20). $L_y = 0.25 L_x = 400$ km.

22 cm/sec in the western part of the southwestern gyre where it merges with the western intensification, and in the western part of the stationary meander between the two dominant gyres. The most unstable eigenmode (Fig. 8) at $\nu = 240\ \mathrm{m^2/sec}$ has a period of 949 days. It is localized in the western half of the basin and it contains several westward propagating eddies. The eigenmode can be interpreted as a zonal wobbling of the positions of the meanders in the southern jet and an associated zonal squashing and stretching of the recirculating gyres. The energy conversion P of the eigenmode (Fig. 9) has maxima associated with the western part of and near the crest of the meander between the southwestern and central gyres, suggesting that the instability is primarily a local instability of the meander. This is similar to the instability of a barotropic circulation in a $\delta = 0.5$ basin (MB1). The period of the normal mode of the quiescent basin with an

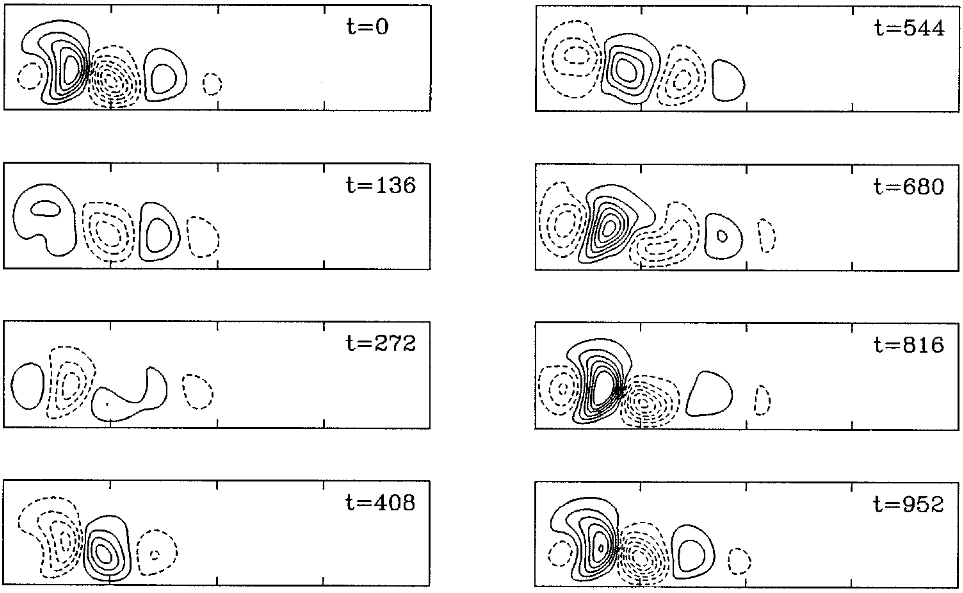

Figure 8. Time-dependent behavior of the streamfunction of the most unstable eigenmode at $\nu = 240\ \mathrm{m^2/sec}$ over one period. $L_y = 0.25 L_x = 400$ km. Time t is measured in days.

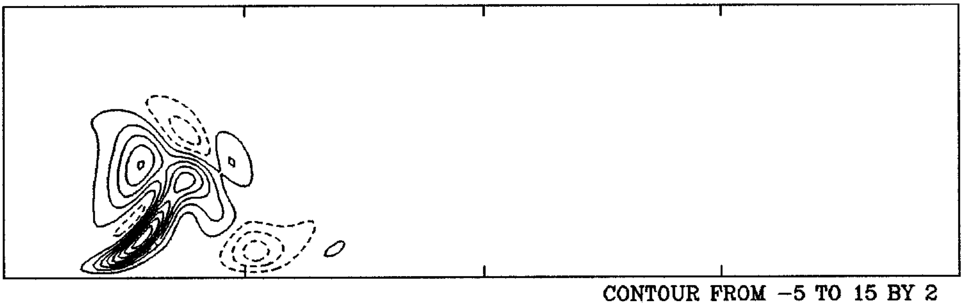

Figure 9. The spatial distribution of the energy conversion term P for the most unstable eigenmode at $\nu = 240\ \mathrm{m^2/sec}$ ($\mathrm{CI} = 2 \times 10^{-6}$). $L_y = 0.25L_x = 400$ km.

x-wavelength of 400 km and a y-wavelength of 800 km (i.e., the basin mode with spatial structure closest to that of the eigenmode shown in Fig. 8) is 940 days, which is close to the 949-day period of the instability. Resonance between the unstable eigenmode and the basin mode may be responsible for the low value of Re_c when compared to the $\delta = 0.5$ case, c.f. MB2.

e. *Discussion*

In the EB model, when the basin is sufficiently large, the near-critical circulations have five cyclonic recirculations of unequal strengths located in the southwest of the basin and a southern boundary current with stationary meanders. The maps of eddy energy production show that the primary instability is associated not with the strongest (the southwestern-most) recirculation or the western boundary current, but with the largest stationary southern meander and a weak recirculation near the western boundary, north of the main recirculation. As the meridional extent of the basin is reduced, the developed western boundary current is first lost, then the northern recirculation. The reduction in length of the developed western boundary current has little effect on the primary instability threshold corroborating the results of the energy analysis which suggests that the developed western boundary current has little to do with the instability. In contrast, the loss of the northern recirculation significantly stabilizes the flow (e.g., going from $\delta = 1$ to $\delta = 0.5$) confirming the conclusion drawn from the energy analysis that the northern recirculation is an important factor in the instability of the EB circulations. Once the northern recirculation is removed, the seat of instability moves to the westward part of the southwestern recirculation gyre and Re_c increases. (Because the meridional gradient of potential vorticity for an approximately zonal flow, $U(y)$ can be written as $\beta + R_D^{-2}U - U_{yy}$, the inflexion point theorem (Pedlosky, 1987) suggests that a westward upper ocean jet tends to be less stable than an eastward upper ocean jet.)

The lack of active energy conversion in the western boundary current and main inertial recirculation gyre of the circulation in an EB basin suggests that a recirculating gyre with an azimuthal velocity structure similar to that of the southwestern recirculation and an EB

Munk boundary layer both are relatively stable when examined as isolated features (c.f. Sections 5 and 6).

The occurrence of a low stability threshold when the frequency of the least damped complex eigenmode is close to the frequency of an eigenmode of the stationary basin demonstrates the destabilizing effect of resonances with basin modes. A similar phenomenon was observed in a barotropic problem (MB1). This effect is probably exaggerated in models such as ours where the simple geometry favors resonances. In a more realistic basin with complex coastal and seafloor geometry (and a finite depth!), it may be more difficult to excite basin modes.

4. Primary instability of the wind-driven baroclinic circulation

When the stratification is represented by a two-layer model, baroclinic instability becomes possible, and the local stability properties of the various flow features that make up a given steady circulation will change as we go from the EB model to the two-layer quasi-geostrophic (2LQG) model, making it likely that the structure of global instabilities and their dependence on basin geometry will also change. These changes are investigated here. First, we describe the instabilities seen in basins with four different geometries. A short comparative discussion of these instabilities follows at the end of the section.

The energy of a basic state of the 2LQG system, described by streamfunctions, $\Psi_1(x, y)$ and $\Psi_2(x, y)$ (Pedlosky, 1987), is the sum of the kinetic and the available potential energies of the flow:

$$E(x, y) = \sum_{i=1,2} \frac{H_i}{H} \frac{|\nabla \Psi_i|^2}{2} + \frac{S\gamma}{2(1+\gamma)^2} (\Psi_2 - \Psi_1)^2. \tag{13}$$

The slowly varying energy density of weakly growing or decaying perturbations $\psi'_{1,2}(x, y, t)$ is

$$\langle E' \rangle = \sum_{i=1,2} \frac{H_i}{H} \left\langle \frac{|\nabla \psi_i|^2}{2} \right\rangle + \frac{S\gamma}{2(1+\gamma)^2} \langle (\psi'_2 - \psi'_1)^2 \rangle. \tag{14}$$

The energy conversion in the baroclinic 2LQG model (Appendix C) may be represented by two terms, each of which corresponds to one physical aspect of the instability. The energy exchange between the basic flow and the perturbations that is due to work done by Reynolds stresses is

$$P = -\varepsilon \sum_{i=1,2} \frac{H_i}{H} \langle \psi'_{ix} J(\psi'_i, \Psi_{ix}) + \psi'_{iy} J(\psi'_i, \Psi_{iy}) \rangle. \tag{15a}$$

The energy exchange associated with a divergent eddy heat flux is

$$R = -\varepsilon \frac{S\gamma}{(1+\gamma)^2} \left\langle (\psi'_1 - \psi'_2) J\left(\frac{1}{2} [\psi'_1 + \psi'_2], \Psi_1 - \Psi_2 \right) \right\rangle. \tag{15b}$$

Table 3. Re_c, ν_c and T_c for the onset of instability in two-layer basins of size $L_x \times L_y$.

L_y (km)	L_x (km)	Re_c	ν_c ($m^2\ s^{-1}$)	T_c (days)
1600	800	36	351	105
800	800	44	283	111
400	800	56	222	120
400	1600	44	281	102

These may act in concert or in opposition. The forms of the exchange terms are not unique, and in choosing (15a,b) we follow BM2.

We explore the most unstable eigenmodes and the energy conversion terms P and R associated with them in the same basins which were used for the EB model. The parameter values are summarized in Table 1 and are motivated by the structure of the Black Sea and continuity with BM2. Some of the critical values are summarized in Table 3.

a. Basin with $L_y = 2L_x = 1600$ km

In the basin with $L_y = 2L_x = 1600$ km, a supercritical Hopf bifurcation occurs at a ν_c located between 350 and 352 m²/sec ($Re_c = UL_x/\nu \simeq 36$). In the unstable steady state (Fig. 10) at $\nu = 350$ m²/sec, the lower layer is at rest. Because the Re_c value is lower than that in the corresponding EB case, the upper layer flow is significantly less nonlinear than that in Figure 2; however, the western boundary current is still well developed, and the southern part of the basin contains two cyclonic gyres. The western recirculation (following the terminology used in Section 3) is more elongated in the meridional direction. The central and eastern recirculations (following the same terminology) are not discernible. The typical velocity of the western boundary current is about 20 cm/sec and its typical width is about 80 km. The velocity in the region where the western boundary current merges with the southwestern gyre reaches 28 cm/sec. The interior of the basin is occupied by northward Sverdrup flow with a typical velocity of about 1.6 cm/sec.

The eigenmode (Fig. 11) consists of a sequence of baroclinic vortices occupying the southern half of the western boundary current and the southwestern corner of the basin. The vortices propagate southward near the western boundary and are advected around the southwestern recirculation gyre. The eigenmode is very different from the EB instability (Section 3) in the same basin. The spatial distribution of the barotropic energy conversion term P (Fig. 12b) also differs from that found at the onset of the EB circulation instability. The maxima of R (Fig. 12a) and P are located near the western boundary, and the area integrals of R and P over the basin are both positive numbers with similar magnitudes. The instability shares the character of both barotropic instability, which feeds on horizontal velocity shear, and baroclinic instability, which draws on vertical velocity shear. This is thus a mixed-mode instability. The structure of the eigenmode and the spatial distribution of the energy conversion terms imply that a mixed instability *of the western boundary current* is responsible for the primary Hopf bifurcation of the flow, although the southwestern gyre and the southern basin boundary distort the eigenmode structure, and the

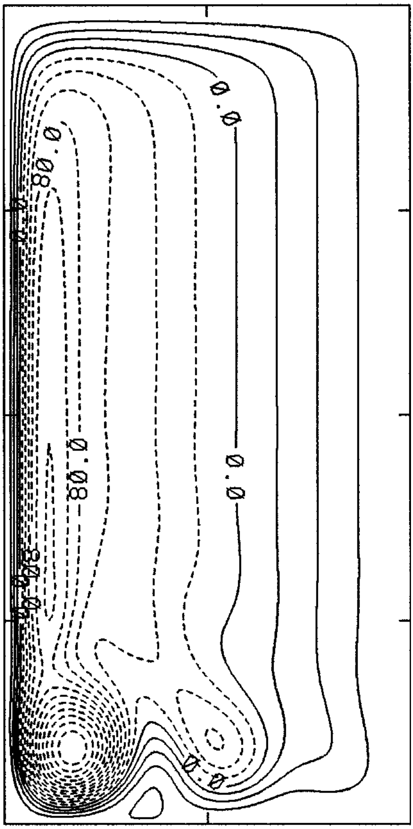

Figure 10. The upper layer streamfunction of the unstable baroclinic steady state at $\nu = 350\ \mathrm{m^2/sec}$ (CI = 20). $L_y = 2L_x = 1600$ km.

southwestern gyre contributes slightly to the energy balance of the mode. An idealized stability problem of the 2LQG western boundary current in an unbounded north-south channel will be discussed in Section 5B and it will be shown there that the bifurcation here is consistent with a local instability of the western boundary current.

The baroclinic conversion rate (Fig. 12a) is largest in a meridional band in the western boundary current. The barotropic conversion rate (Fig. 12b) is largest in a meridional band offshore of the baroclinic maximum. This band is centered on the longitude at which the meridional velocity in the western boundary layer is zero. (There is a weak northward flow to the east of it, part of the standard Munk boundary layer solution.) The longitudinal localization of the baroclinic conversion rate is consistent with the eigenmode structure seen in Figure 11. The eddies in the upper layer are tilted more toward a NW-SE orientation than those in the lower layer, and therefore the phase difference between the upper and lower eddies changes as one moves offshore. This is close to $\pi/2$ next to the western boundary, $\pi/4$ in the middle of the western boundary layer; i.e., favorable for the release of

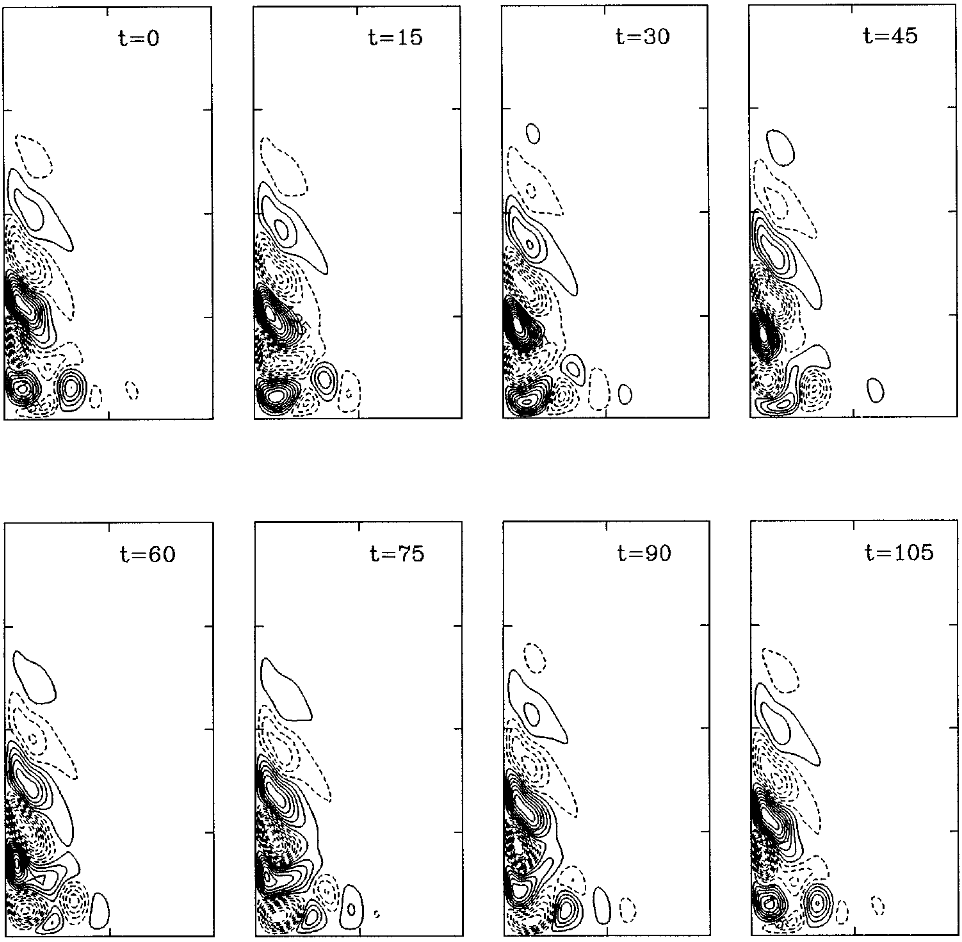

Figure 11. Time-dependent behavior of the streamfunctions of the most rapidly growing eigenmode at $\nu = 350$ m^2/sec over one period. $L_y = 2L_x = 1600$ km. Time t is measured in days. (a) The upper layer (b) The lower layer.

potential energy, and close to zero; i.e., relatively barotropic, at the outer edge. Further, the NW-SE tilt of the upper layer eddies increases toward the outer edge of the jet, rendering them more effective at extracting energy from the horizontal shear there.

The southward increase in the magnitude of the conversion terms arises because the instability is a spatially growing instability of the western boundary current; eddies grow as they propagate southward until they reach the southwestern gyre. (The western boundary current is convectively unstable for a range of Reynolds numbers below Re_c; the critical Reynolds number for the onset of the temporal instability corresponds to the transition of the western boundary current instability from a convective instability to an absolute instability.)

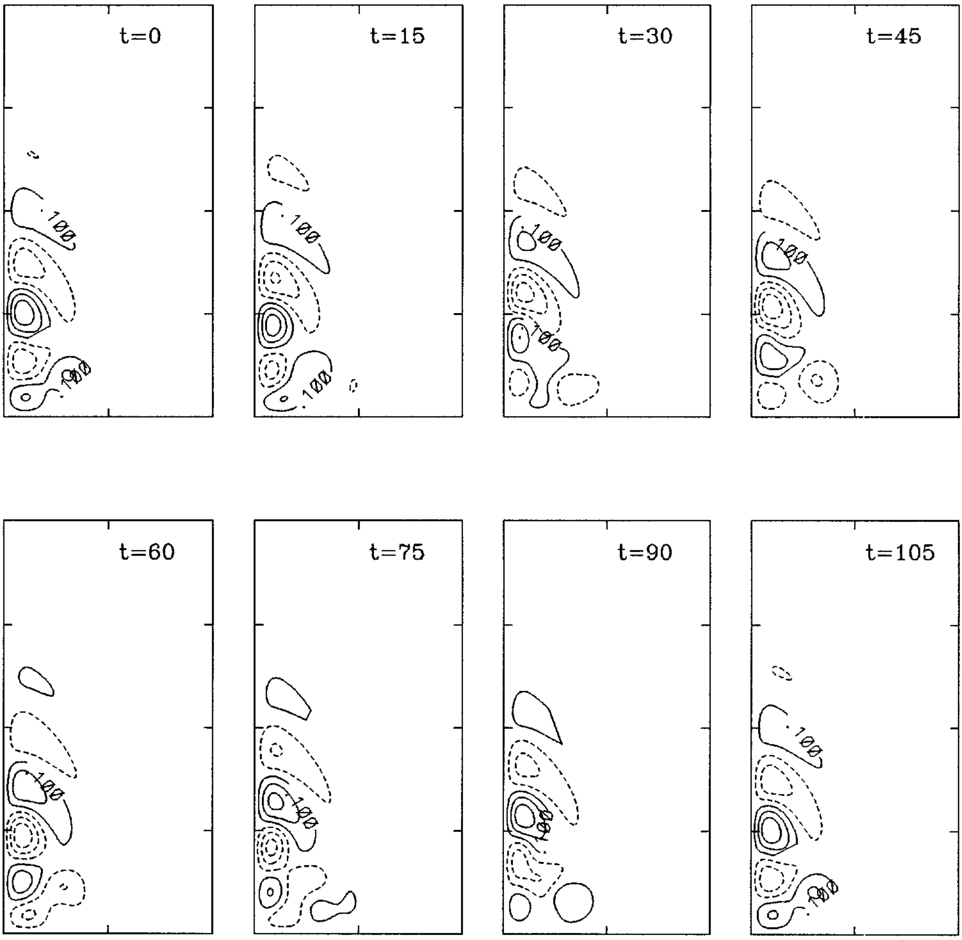

Figure 11b (continued).

b. Basin with $L_y = L_x = 800$ km

In the basin with $L_y = L_x = 800$ km, a Hopf bifurcation occurs at a value of ν_c located between 282 and 284 m^2/sec ($Re_c \simeq 44$). The upper layer streamfunction (Fig. 13) of the unstable steady state at $\nu = 280$ m^2/sec has a weak western recirculation, but as in the $\delta = 2$ case, the central and eastern recirculations are not present. The most unstable eigenmode at $\nu = 280$ m^2/sec has a period of 111 days, and energy conversion distributions (Fig. 14) similar to those found for the $\delta = 0.5$ basin in BM2. Exchanges of energy between the basic state and the growing mode occur primarily in the southwestern gyre. The area integral of R is positive, whereas the area integral of P is negative, an indication that baroclinic instability is the primary mechanism destabilizing the flow. The period reported in BM2 was 120 days, which is close to what we found here in the square basin; however, the $\delta = 0.5$ basin was more stable, with $Re_c \simeq 56$. These results suggest that the instability

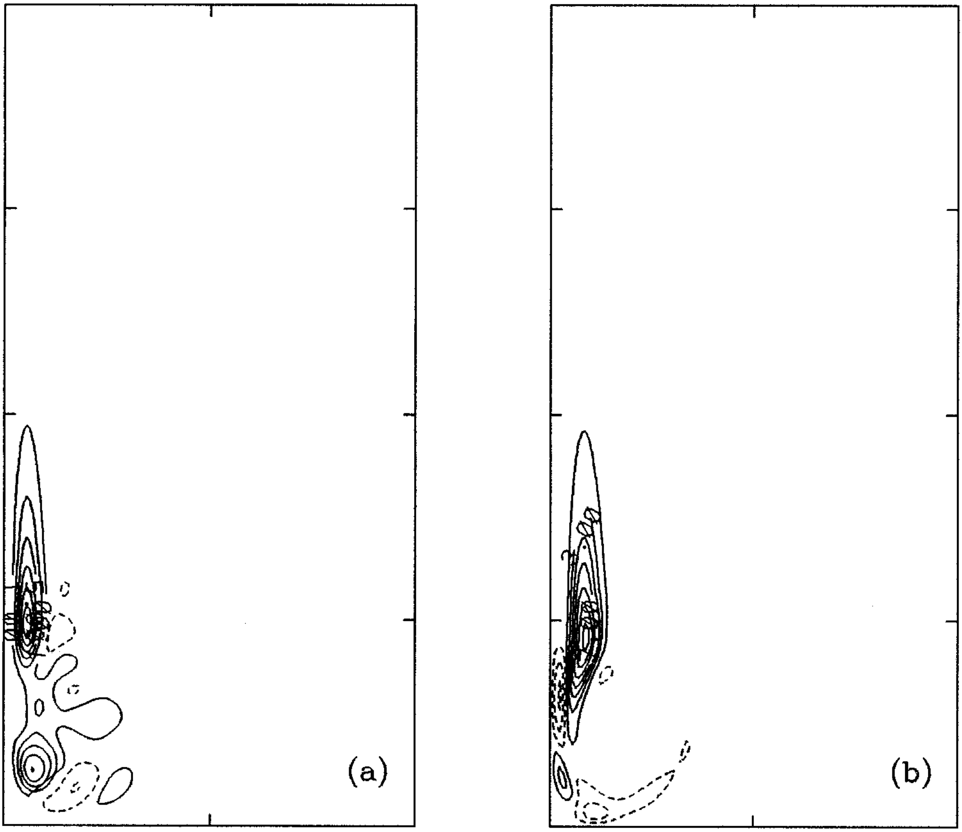

Figure 12. The spatial distribution of the energy conversion terms for the most rapidly growing eigenmode at $\nu = 350$ m^2/sec. $L_y = 2L_x = 1600$ km. (a) R (b) P (CI $= 2 \times 10^{-5}$).

is of the same type as one found in BM2, and that it is a baroclinic instability of the southwestern gyre. The instability resembles an azimuthal mode-two instability of a baroclinic vortex distorted by the basin boundaries and surrounding flow. However, given the appearance around the southwestern gyre (Fig. 14a) of pronounced maxima and minima of R, which is a time-averaged quantity, we conclude that this is not simply a mode-two instability of an isolated vortex. The asymmetries associated with the nearby boundaries and the western boundary current influence the vortex stability.

In Section 6, we solve the viscous instability problem of a circular gyre on an f-plane and show that, given parameters corresponding to the wind-driven circulation model, the second azimuthal mode is the most likely mode to become unstable.

c. *Basin with $L_y = 0.25L_x = 400$ km*

A Hopf bifurcation in the basin with $L_y = 0.25L_x = 400$ km occurs at ν_c between 280 and 283 m^2/sec ($Re_c \simeq 44.4$). The unstable steady state at $\nu = 281$ m^2/sec contains two gyres

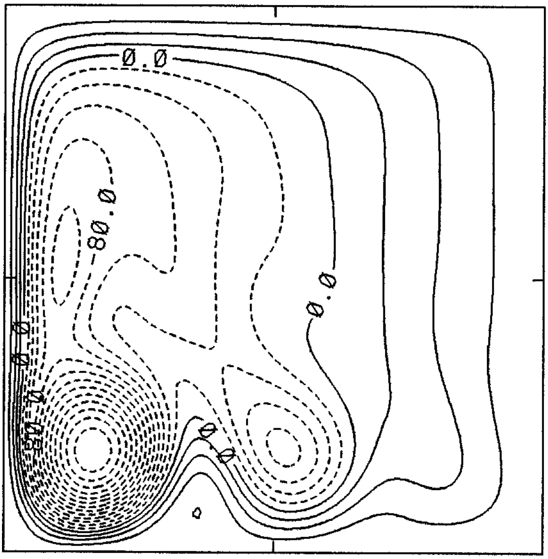

Figure 13. The upper layer streamfunction of the unstable baroclinic steady state at $\nu = 280$ m^2/sec (CI = 20). $L_y = L_x = 800$ km.

and a very weak eastern recirculation in the upper layer (Fig. 15a). The overall pattern is similar to the one described in Section 3 for the EB circulation in the same basin at $\nu =$ 240 m^2/sec. The most unstable eigenmode (not shown) has a period of 102 days and, like the $\delta = 1$ case above, is rather similar to the one found in a basin with $\delta = 0.5$ (BM2), although in the present case the westward jet in the northern part of the basin also plays a role in the instability process. This can be seen in the spatial pattern of the energy conversion terms computed for the growing eigenmode (Fig. 15b,c). The maxima of the baroclinic conversion R are associated with the southwestern gyre and the westward jet in the northern part of the basin. The main maximum of R is located in the northwestern corner of the basin, where the jet accelerates up to 8 cm/sec, turns south-west and begins to merge with the south-western gyre. The barotropic energy exchange is weak in comparison to the baroclinic exchange, and when integrated over the basin, the net barotropic exchange is a small negative number. This suggests that, once again, baroclinic instability is the main mechanism destabilizing the flow with instability of the confluent flow in the northwestern part of the basin predominating.

d. Discussion

The results of Section 4 highlight a number of differences between the reduced gravity model of the thermocline and the two-layer model. At each aspect ratio examined, the baroclinic flow is more unstable; i.e., unstable at a lower Reynolds number than the equivalent barotropic flow. This difference is least when the meridional extent is smallest. For the equivalent barotropic flow, the most unstable flow of the four examined here is the

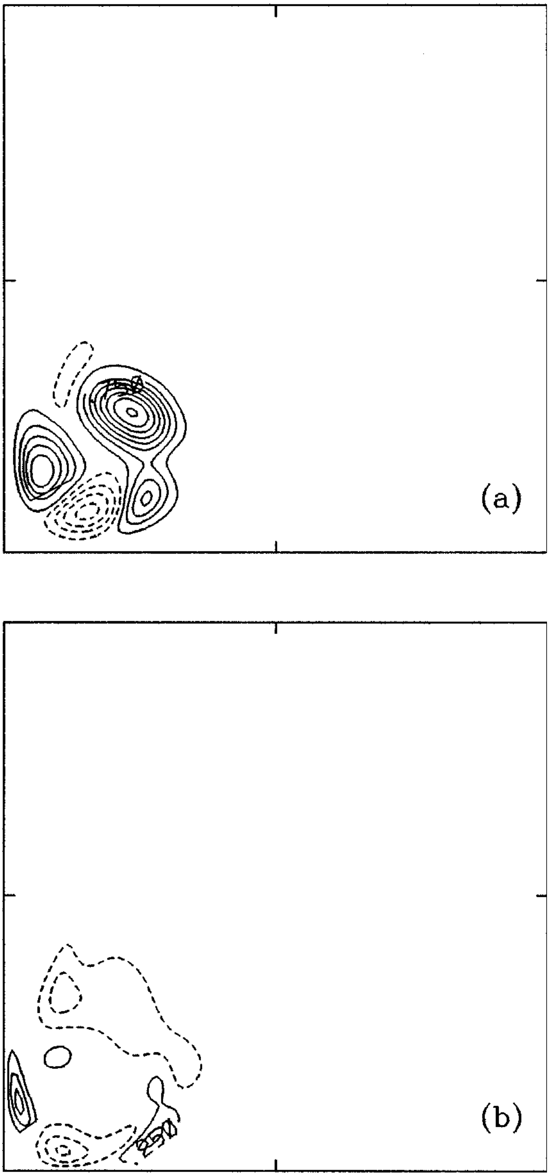

Figure 14. The spatial distribution of the energy conversion terms R and P for the most unstable growing eigenmode at $\nu = 280$ m^2/sec. $L_y = L_x = 800$ km (CI $= 0.5 \times 10^{-6}$).

one in the basin with the least meridional and largest zonal extent. For the baroclinic flows, the opposite is true; the most unstable flow is the one in the basin with the largest meridional extent. In part this is due to a change in the preferred mode of instability; when the meridional extent of the western boundary current is sufficiently large, the primary

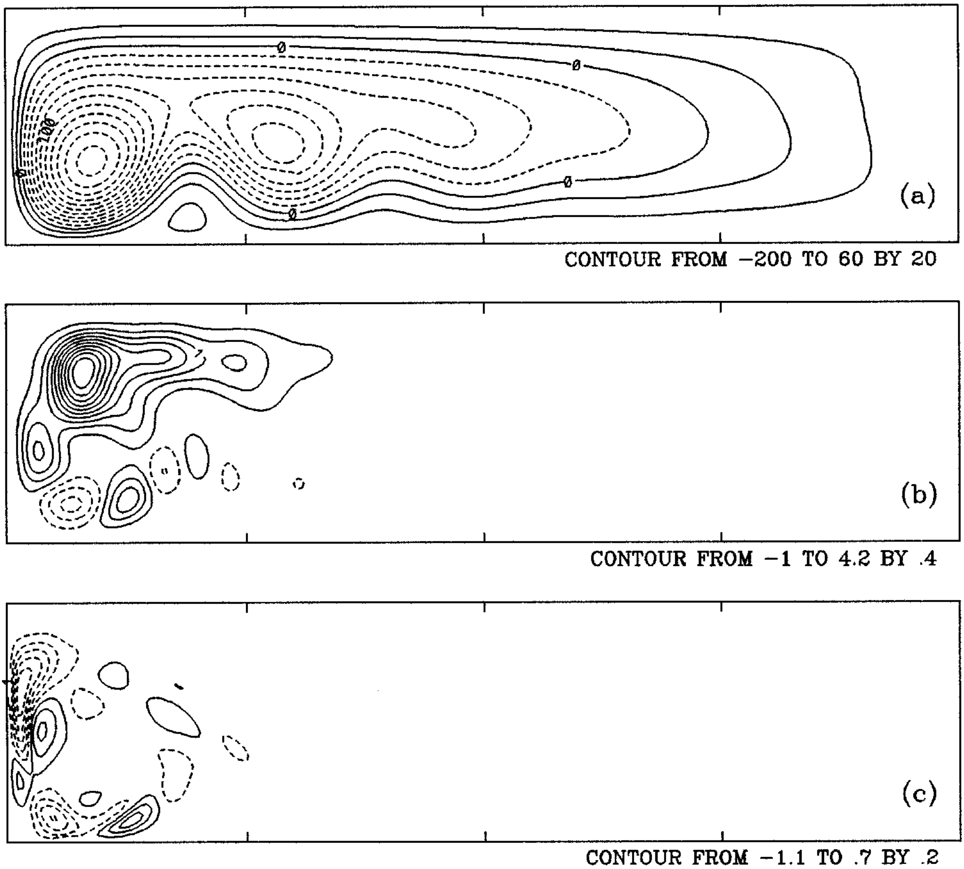

Figure 15. The unstable baroclinic steady state and the energy conversion terms at $\nu = 280$ m^2/sec. $L_y = 0.25L_x = 400$ km. (a) The upper layer streamfunction (CI = 20); (b) The baroclinic energy conversion R of the most unstable eigenmode (CI = 0.4×10^{-6}); (c) The barotropic energy conversion P of the most unstable eigenmode (CI = 0.2×10^{-6}).

instability of the baroclinic circulation is a western boundary current instability that draws upon both the vertical and horizontal shear in the boundary current. When the western boundary current is too short, instability of the baroclinic general circulation first occurs as a baroclinic instability of the southwestern recirculation, or, in the case of the basin of very small meridional extent and large zonal extent, from baroclinic instability of the southwestern recirculation and the westward zonal boundary current.

The instabilities of the equivalent barotropic problem are, of course, due to the horizontal shears, but the part of the circulation that drives the instability changes with the basin aspect ratio. For aspect ratios of $\delta = 2$, 1, and 0.25, the standing meander between the main inertial recirculation gyres is an active site of energy conversion from the basic flow to the unstable mode. This was also the case in the homogeneous ocean model of MB2 when the meridional extent was 1024 km or less. However, a big difference between the equivalent barotropic and true barotropic circulations is that, like the baroclinic case, the western boundary current is the primary source of instability in the barotropic flow when the basin has a meridional extent of 2048 km. In contrast to the primary instabilities of the EB flow, the standing meander between the dominant gyres of the baroclinic model is not associated with a maximum of the energy conversion, which suggests that it is not a source of instability at least as far as the primary instabilities are concerned. Like the instability of the equivalent barotropic double-gyre problem seen by Jiang *et al.* (1995), the spatial structure of the primary instability in the equivalent barotropic problem appears relatively complex, whereas the baroclinic instabilities seem more straightforward (except for the $\delta = 0.25$ case); it is usually easy to identify the latter instabilities with a particular flow feature. This difference in the structure of the instabilities of the equivalent barotropic and baroclinic circulations is most easily seen in the spatial patterns of the energy conversion terms, Figures 1b, 4, 6, 9, 12 and 14.

5. Viscous instability of western boundary currents

In order to illuminate the instabilities described in Sections 3 and 4 we look next at the viscous instability properties of western boundary currents and circular vortices. Our main purposes will be to verify the local character of the instabilities seen in the GCMs and provide physical insight into the instability processes through a significant physical simplification of the problem at hand. We will isolate the main "sources" of the instability: the western boundary current and the southwestern recirculation gyre, leaving the standing meander beyond the scope of our study. The main reason for not considering the meander was computational. Thanks to symmetry, stability problems of a circular gyre and a boundary current in an unbounded channel can be reduced to one-dimensional problems, but the stability of a meander (or train of meanders) is an essentially two-dimensional question. In Section 5 we look into the stability of the EB and 2LQG western boundary currents and connect the results with GCM solutions.

a. The equivalent-barotropic western boundary current

We denote the upper layer depth by H_1 and the reduced gravity by g'. The linearized equation of motion for the perturbation ψ_1 of the basic state streamfunction Ψ_1 is

$$\frac{\partial}{\partial t}\left(\nabla^2\psi_1 - \left(\frac{1}{R_d^2}\right)\psi_1\right) + J(\Psi_1, \nabla^2\psi_1) + J(\psi_1, \nabla^2\Psi_1) + \beta_0\frac{\partial\psi_1}{\partial x} = \nu\nabla^4\psi_1, \qquad (16)$$

where $R_d = \sqrt{g'H_1}/f_0$—the deformation radius, ν—the eddy viscosity coefficient and β_0 is the derivative of the Coriolis parameter. The basic state we choose (to be specified below) is a meridional flow with no y-dependence. The dimensional parameters are Ψ_0—a characteristic value of the basic state streamfunction, R_d, ν and β_0. We introduce the following nondimensional parameters: $Re = \Psi_0/\nu$—the Reynolds number, $\delta_M =$

$(\nu/\beta_0)^{1/3}$—a viscous boundary layer length scale and $S = (\delta_M/R_d)^2$—a measure of the stratification. We nondimensionalize by taking δ_M to be the length scale; Ψ_0/δ_M to be the velocity scale and δ_M^2/Ψ_0, the time scale. (Note that in Section 5, we have a velocity scale Ψ_0/δ_M that is appropriate to the flow in the western boundary current, while in the wind-driven models described in Section 2 the velocity scale was specified from the Sverdrup balance. Because of the form of the Munk solution, we implicitly choose Ψ_0 to be $\tau_0/\rho H_1\beta_0$. The Reynolds numbers may then be compared to those in Section 3.) The nondimensionalization of (16) gives

$$Re\left(\frac{\partial}{\partial t}(\nabla^2\psi_1 - S\psi_1) + \overline{U}\nabla^2\psi_{1y} - \overline{U}_{xx}\psi_{1y}\right) + \psi_{1x} = \nabla^4\psi_1, \tag{17}$$

where $\overline{U}(x) = \Psi_{1x}$ is the basic state velocity and all variables are nondimensional. We apply a normal mode analysis to (17), looking at perturbations of the form

$$\psi_1(x, y, t) = e^{i\alpha(y-\lambda t)}\tilde{\psi}(x) + e^{-i\alpha(y-\lambda^* t)}\tilde{\psi}^*(x). \tag{18}$$

The substitution of (18) into (17) yields an equation similar to the Orr-Sommerfeld equation

$$\tilde{\psi}^{IV} - 2\alpha^2\tilde{\psi}'' - \tilde{\psi}' + \alpha^4\tilde{\psi} - i\alpha Re[(\overline{U} - \lambda)(\tilde{\psi}'' - \alpha^2\tilde{\psi}) - \overline{U}_{xx}\tilde{\psi} + \lambda S\tilde{\psi}] = 0. \tag{19}$$

We choose the western boundary of the channel to be at $x = 0$, and the eastern one at $x = w$. Then, the boundary conditions for $\tilde{\psi}$ are

$$\tilde{\psi}(0) = \tilde{\psi}(w) = \tilde{\psi}_x(0) = \tilde{\psi}_x(w) = 0, \tag{20}$$

i.e., no-flow through and no-slip past the lateral boundaries of the channel. Eq. (19) with the boundary conditions (20) is an eigenvalue problem for λ with control parameters Re, S, w and α (the wavenumber of the normal mode). The eigenvalue problem (19) was solved numerically (Appendix A).

Following Ierley and Young (1991), (IY), we chose the Munk profile for the basic velocity $\overline{U}(x)$. The nondimensional expression for $\overline{U}$ is

$$\overline{U} = e^{-x/2}\sin\left(\frac{\sqrt{3}x}{2}\right). \tag{21}$$

Comparing results for $w = 50$ with those for $w = \infty$, IY showed that when $w = \infty$, the basin modes disappear from the spectrum, but the most unstable trapped modes remain essentially unchanged. We kept the width of the channel fixed and large, compared to the x-scale of the trapped modes, by setting $w = 50$.

We computed the marginal stability curves for a set of different S. In the barotropic limit, $S \rightarrow 0$ ($R_d \rightarrow \infty$). The marginal curves were found for the barotropic case (repeating a result in IY) and $S = 0.0457, 0.1828, 0.3730, 0.4911$ and 0.7310 (see Fig. 16). The "nose" of the

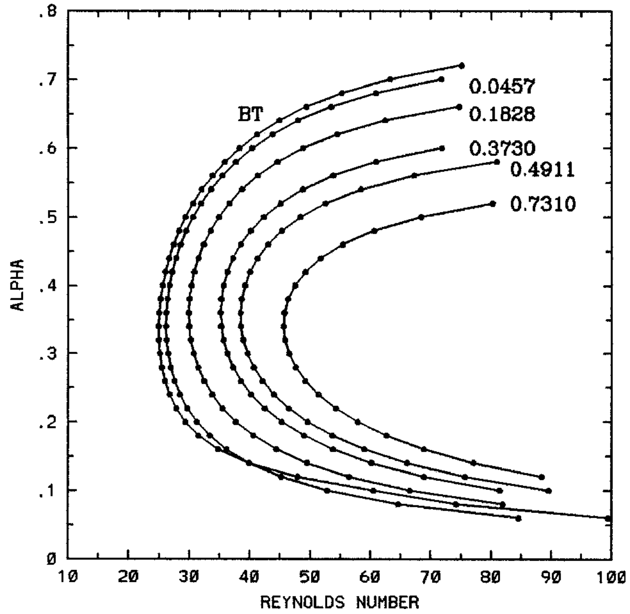

Figure 16. Marginal stability curves of the EB western boundary current in the unbounded channel. $S = 0, 0.0457, 0.1828, 0.3730, 0.4911$ and 0.7310.

barotropic curve is located at $Re_c = 24.9$ and $\alpha_c = 0.335$. Whereas α_c is in a good agreement with the value 0.3359 found by IY, our Re_c is slightly higher than the 21.574 reported in IY.

As Figure 16 shows, the stability of the boundary current grows as S is increased (R_d is reduced). The last two points on the barotropic marginal curve at $\alpha = 0.06, 0.08$ correspond to the destabilized basin modes (really, channel modes) discussed by IY. In the nonzero S cases, the basin modes are always more stable than the trapped modes over the range of wavenumbers examined. The variation of λ versus α along the marginal stability curves (Fig. 17) is such that the period of the critical modes increases (λ decreases) as S is increased. For $S = 0.658$, the value used in Section 3 for the basin with $\delta = 2$: $Re_c = 43.3$, $\alpha_c = 0.347$ (in dimensional form $\alpha_c = 2\pi/18.11\delta_M$) and $\lambda_c = 0.1092$.

The stabilization of the flow associated with an increase in S occurs not only for the idealized western boundary currents in an infinite meridional channel. In Section 3, when we computed the unstable steady states of the EB model (except for the EB case with $\delta = 2$) we used a stabilizing technique (Appendix A) based on an artificial reduction of R_d (an increase of S). The fact that this technique worked for the different kinds of instability suggests that increasing S has a more general stabilizing effect on the circulation and that this effect is not limited to the western boundary currents.

In Figure 18, we show the marginally stable eigenfunctions $\tilde{\psi}$ (each eigenfunction is presented as $|\tilde{\psi}|e^{i\Phi}$; amplitude $|\tilde{\psi}|$ and phase Φ are shown in different panels) computed at

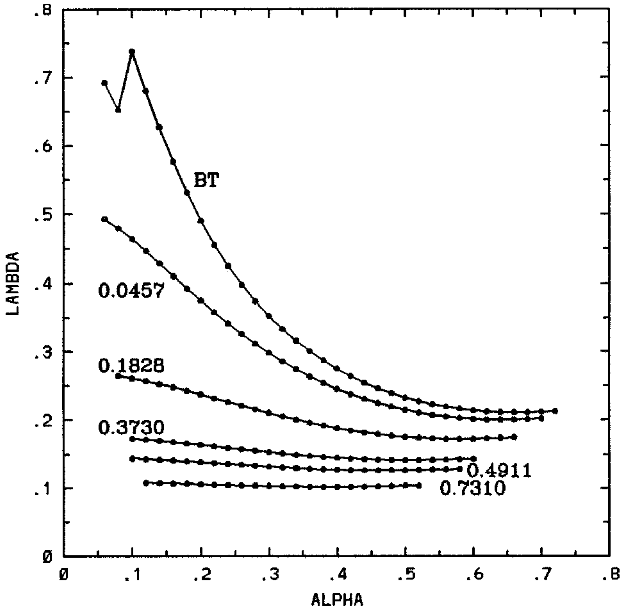

Figure 17. Variation of λ versus α for the marginal stability curves computed at $S = 0$, 0.0457, 0.1828, 0.3730, 0.4911 and 0.7310. The last two points at $\alpha = 0.06, 0.08$ for $S = 0$ correspond to a destabilized basin mode rather than a localised shear instability.

the "noses" of the marginal curves (the critical modes) corresponding to $S = 0.0457$ and 0.7310. The eigenfunctions are trapped at the western boundary and have oscillatory tails that decay as one moves eastward analogously to what was found by IY for the barotropic case. The shorter is the deformation radius R_d (the larger S), the more trapped are the eigenfunctions (Fig. 18a,c). Outside the boundary current, the phase of the eigenfunction with $S = 0.0457$ may be approximated as $\Phi \sim -0.21x$. In the case of $S = 0.7310$, it is approximately $\Phi \sim -0.33x$. This indicates that for the shorter R_d, the scale of the oscillation in the far-field also becomes shorter. Eigenmodes with shorter x-scale are more damped by the lateral dissipation. This may account for the growth of Re_c associated with an increase in S (decrease in R_d).

b. Comparison with instabilities seen in the EB GCM

The period of the marginal eigenmode for $S = 0.658$ (the value used in Section 3 for the EB circulation in the basin with $\delta = 2$) is $T = 2\pi/\alpha\lambda_c = 165.8$. The dimensional period can be obtained by multiplying this value by the time scale $[T] = \delta_M^2/\nu Re$. Using $\delta_M = 19.79$ km and $\nu = 155$ m^2/sec, as for the EB circulation with $\delta = 2$, this gives $T_{dim} = 112.0$ days. The difference between this period and the period of 687 days found in the EB model with $\delta = 2$ is significant.

Although, the western boundary layer may become unstable in a basin with $L_y >$

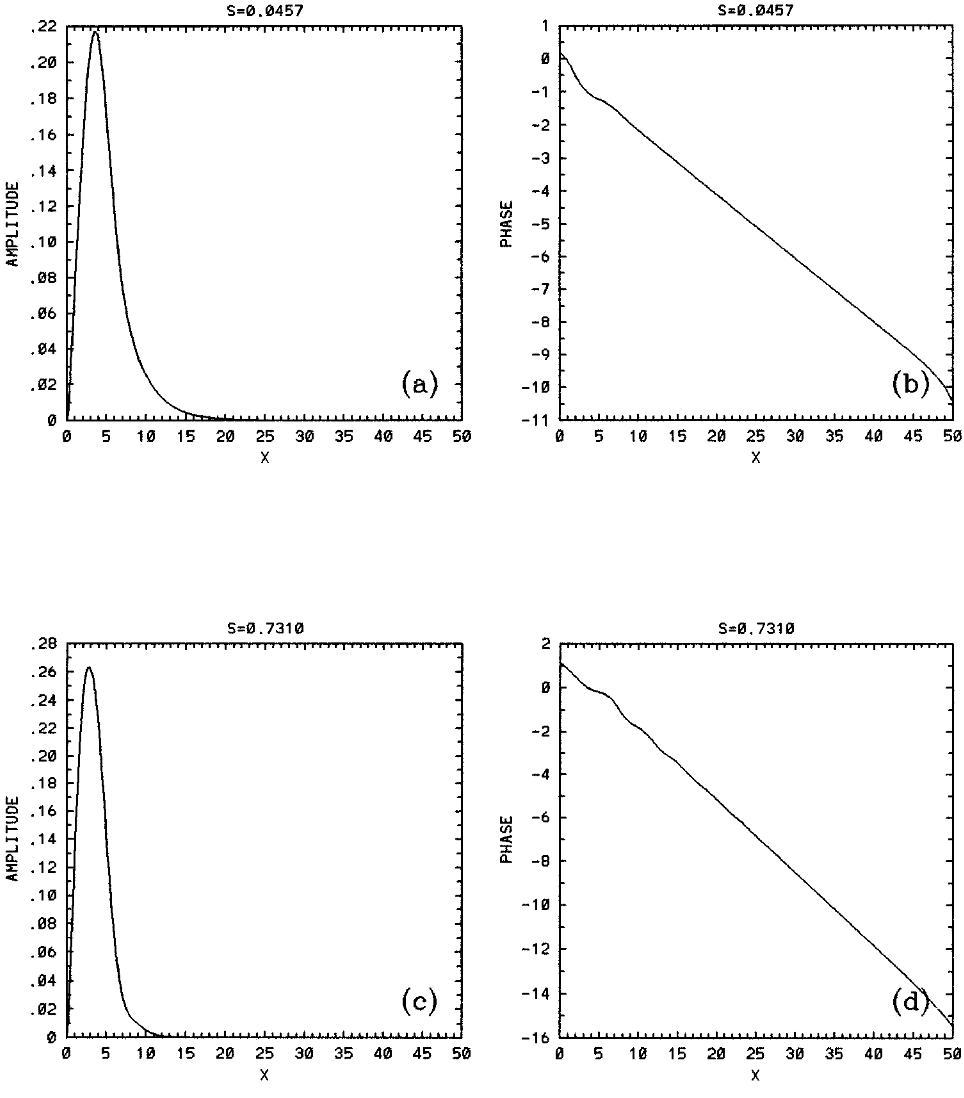

Figure 18. Amplitudes and phases of the critical eigenmodes $\tilde{\psi}(x)$ at Re_c (located at the "noses" of the marginal curves). (a) $S = 0.0457$; (b) $S = 0.7310$. For greater S, the eigenmode becomes more trapped at the western boundary.

1600 km (we found a western boundary layer instability in an EB basin with $L_x = 800$ km and $L_y = 2400$ km), this does not happen in the basins with $L_y = 1600$ and 800 km. The structure and period of the most unstable eigenmode computed in the EB GCM with $\delta = 2$, and the energy conversion associated with the eigenmode do not suggest an instability of the boundary layer. A different mechanism is responsible for the onset of instability in the solutions from Section 3. This is despite the fact that the critical Reynolds number seen in the EB GCM is larger than the critical *Re* of the western boundary current instability in the $S = 0.658$ channel. The inferred stabilization of the western boundary current in the GCM can be explained by the influence of the zonal boundaries and subsequent distortion of the current by the gyres and weaker recirculations. Also, the limited length of the western boundary current makes it difficult for an along-jet mode to grow. For $S = 0.658$ the along-jet wavelength is $18.11\delta_M \simeq 360$ km and, therefore, only a few spatial periods will fit in a basin with $L_y = 1600$ km (the developed western boundary current is always shorter than L_y).

The unbounded channel problem gives a useful insight into a possible mechanism of instability (we found this instability in a basin with $L_y = 2400$ km), but it does not account for the complexity of the two-dimensional circulation in smaller basins and does not predict the form of the primary instability in such basins.

c. The baroclinic western boundary current

We model a baroclinic western boundary current in an unbounded north-south channel using the 2LQG approximation. The upper and lower layer depths are denoted H_1 and H_2 (the EB current studied in (a) had $H_2 \to \infty$). The basic state upper layer streamfunction Ψ_1 is again taken to be the Munk velocity profile (21) and the lower layer is at rest in the basic state: $\Psi_2 = 0$. We chose the lower layer to be at rest in the basic state for consistency with the baroclinic steady states of Section 4 which have no-flow in the lower layer. The linearized governing equations for the perturbation streamfunctions $\psi_{1,2}$ are

$$\frac{\partial}{\partial t}\left(\nabla^2\psi_1 - \frac{1}{(1+\gamma)R_d^2}(\psi_1 - \psi_2)\right) + J\left(\Psi_1, \nabla^2\psi_1 + \frac{1}{(1+\gamma)R_d^2}\psi_2\right) + J(\psi_1, \nabla^2\Psi_1) + \beta_0\frac{\partial\psi_1}{\partial x} = \nu\nabla^4\psi_1 \tag{22}$$

$$\frac{\partial}{\partial t}\left(\nabla^2\psi_2 - \frac{\gamma}{(1+\gamma)R_d^2}(\psi_2 - \psi_1)\right) + J\left(\psi_2, \frac{\gamma\Psi_1}{(1+\gamma)R_d^2}\right) + \beta_0\frac{\partial\psi_2}{\partial x} = \nu\nabla^4\psi_2,$$

where $\gamma = H_1/H_2$ is the layer depth ratio and $R_d = (\sqrt{g'}/f_0)\sqrt{H_1H_2/(H_1 + H_2)}$. We nondimensionalize (22) in the same way as in subsection (a) for Eq. (16), and obtain

$$Re\left[\frac{\partial}{\partial t}\left(\nabla^2\psi_1 - \frac{S}{1+\gamma}(\psi_1 - \psi_2)\right) + \overline{U}\left(\nabla^2\psi_{1y} + \frac{S}{1+\gamma}\psi_{2y}\right) - \overline{U}_{xx}\psi_{1y}\right] + \psi_{1x} = \nabla^4\psi_1$$

$$Re\left[\frac{\partial}{\partial t}\left(\nabla^2\psi_2 - \frac{S\gamma}{1+\gamma}(\psi_2 - \psi_1)\right) - \overline{U}\frac{S\gamma}{1+\gamma}\psi_{2y}\right] + \psi_{2x} = \nabla^4\psi_2. \tag{23}$$

We apply a normal mode analysis to (23), looking at perturbations of the form

$$\psi_{1,2}(x, y, t) = e^{i\alpha(y-\lambda t)}\tilde{\psi}_{1,2}(x) + e^{-i\alpha(y-\lambda^* t)}\tilde{\psi}_{1,2}{}'^*(x). \tag{24}$$

The normal mode decomposition of (23) yields two coupled equations for $\tilde{\psi}_1$ and $\tilde{\psi}_2$:

$$\tilde{\psi}_1^{\mathrm{IV}} - (2\alpha^2 + i\alpha Re\overline{U})\tilde{\psi}_1'' - \tilde{\psi}_1' + (\alpha^4 + i\alpha^3 Re\overline{U} + i\alpha Re\overline{U}_{xx})\tilde{\psi}_1 - i\alpha Re\frac{S}{1+\gamma}\overline{U}\tilde{\psi}_2$$

$$= \lambda i\alpha Re\left(-\tilde{\psi}_1'' + \left(\alpha^2 + \frac{S}{1+\gamma}\right)\tilde{\psi}_1 - \frac{S}{1+\gamma}\tilde{\psi}_2\right) \tag{25}$$

$$\tilde{\psi}_2^{\mathrm{IV}} - 2\alpha^2\tilde{\psi}_2'' - \tilde{\psi}_2' + \left(\alpha^4 + i\alpha Re\frac{S\gamma}{1+\gamma}\overline{U}\right)\tilde{\psi}_2 = \lambda i\alpha Re\left(-\tilde{\psi}_2'' + \left(\alpha^2 + \frac{S\gamma}{1+\gamma}\right)\tilde{\psi}_2 - \frac{S\gamma}{1+\gamma}\tilde{\psi}_1\right),$$

with boundary conditions at $x = 0$ and $x = w$ of:

$$\tilde{\psi}_{1,2}(0) = \tilde{\psi}_{1,2}(w) = \tilde{\psi}'_{1,2}(0) = \tilde{\psi}'_{1,2}(w) = 0. \tag{26}$$

Again, we choose $w = 50$. We solve the eigenvalue problem (25), (26) numerically (Appendix A) using a mesh of 200 points.

The marginal stability curves of the current were computed for the set, $S = 0.0457$, 0.7310, 1.2577, and for $\gamma = \frac{1}{9}, \frac{1}{3}$. The marginal curves $Re(\alpha)$ and plots of λ versus α along the marginal curves for $\gamma = \frac{1}{9}$ (Fig. 19) and $\gamma = \frac{1}{3}$ (Fig. 20) show that Re_c depends only weakly upon S in this range. This is not the case for the EB current which stabilizes as S is increased. The marginal stability curves for $\gamma = \frac{1}{3}$, $\frac{1}{9}$ and 0 (the EB case) are superimposed for $S = 0.0457$ (Fig. 21a) and $S = 0.7310$ (Fig. 21b) showing that Re_c does not change significantly for small S (large R_d), but when S is large (small R_d), Re_c grows as γ is reduced. The second situation is more typical of R_d values used in our GCMs. The change in sensitivity to γ as R_d is varied is because of the mixed nature of the instability. For large R_d, the instability is predominantly barotropic and therefore insensitive to γ while for small R_d, the instability is more baroclinic. When we looked for the unstable steady states in Section 4, we artificially decreased γ in order to stabilize the flow. This suggests that reduction of γ has a more general stabilizing effect on the circulation and that the stabilizing effect is not limited to the western boundary currents.

When R_d is small, the meridional scale of the critical eigenmode slightly increases (α_c decreases) when γ is reduced (Fig. 21b). The period of the critical eigenmode increases slightly (λ decreases) when γ is reduced (Figs. 19b, 20b).

d. Comparison with instabilities seen in the baroclinic GCM

In Section 4, we saw that the steady flow in the 2LQG GCM became unstable near $\nu = 350$ m^2/sec. In the critical steady state, the maximum velocity of the western boundary current is approximately 0.2 m s^{-1}. The maximum velocity in the Munk boundary layer profile (21) is $U_{max} = 0.4731$. We can therefore estimate a local Reynolds number for the western boundary current in the steady state of the 2LQG GCM when $\nu = 350$ m^2/sec and $\delta = 2$, as $Re_l = (0.2/U_{max})(350/\beta_0)^{1/3}(1/350) \approx 31$.

For the Munk boundary layer profile in the infinitely long two-layer channel model,

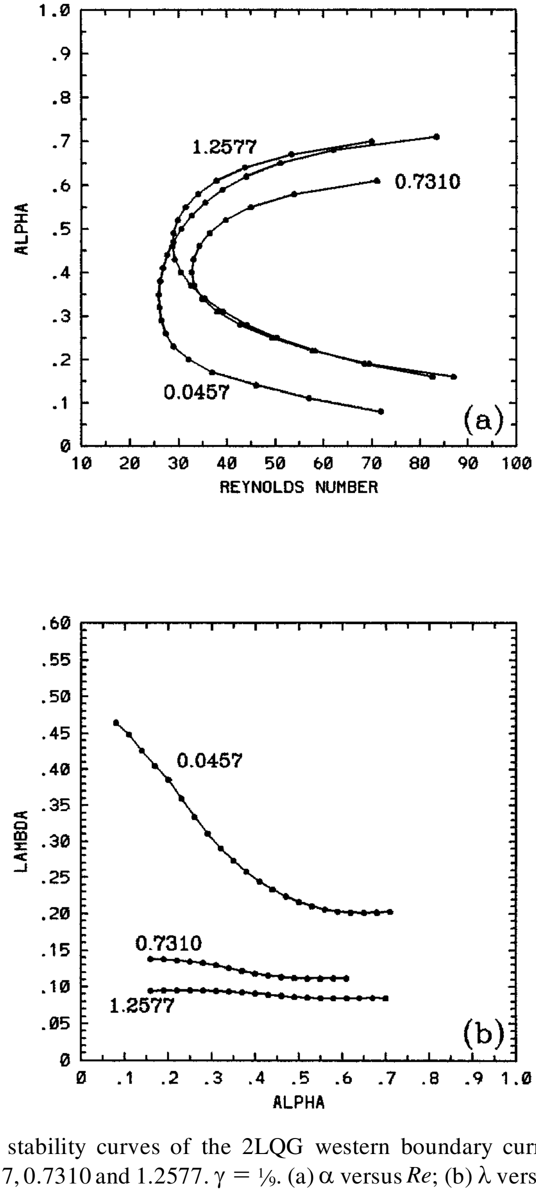

Figure 19. Marginal stability curves of the 2LQG western boundary current in an unbounded channel. $S = 0.0457, 0.7310$ and 1.2577. $\gamma = 1/9$. (a) α versus Re; (b) λ versus α.

when $S = 1.2577$ and $\gamma = 1/9$, parameter values analogous to those used in the GCM, Re_c is 28.7. The corresponding critical eigenmode (Fig. 22) of the channel model has a meridional wavelength of 360 km, which is in good agreement with the wavelength estimated for the eigenmode found in the 2LQG GCM for $\delta = 2$. The period of the critical eigenmode of the process study is 91 days, reasonably close to the 105 day period of the critical eigenmode of the GCM. Some of the discrepancy between the values of Re_c and the

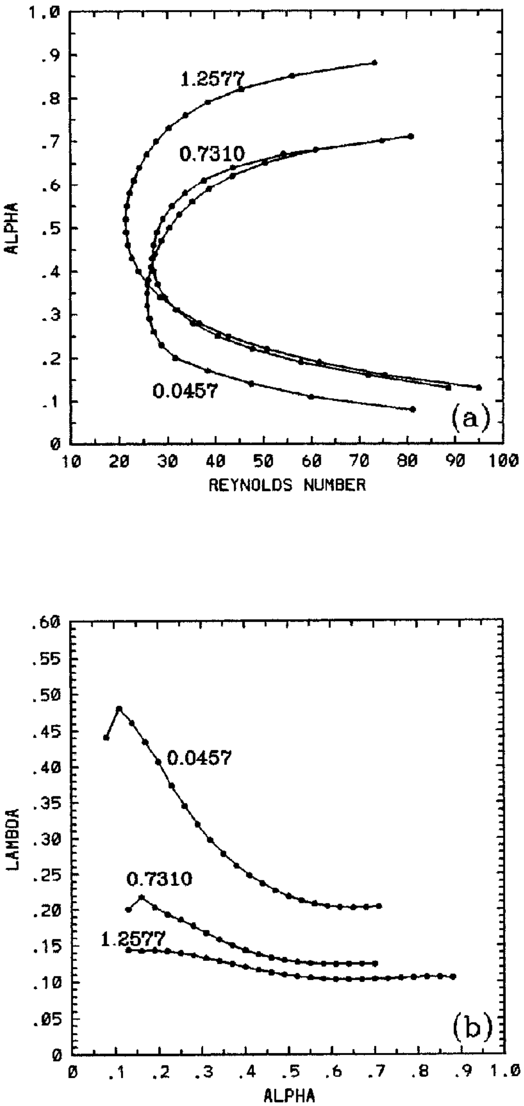

Figure 20. Marginal stability curves of the 2LQG western boundary current in an unbounded channel. $S = 0.0457, 0.7310$ and 1.2577. $\gamma = 1/3$. (a) α versus Re_c; (b) λ versus α. The last points at $\alpha = .08$ for $S = 0.0457$ and at $\alpha = .13$ for $S = 0.7310$ correspond to destabilized basin modes.

periods in the idealized Munk boundary layer problem and the corresponding values in the GCM may be due to the influence of the zonal boundaries of the basin, which impose a finite length on the current. Also, the western part of the southwestern gyre contributes to the instability.

To summarize, the two-layer western boundary current in an meridional channel loses

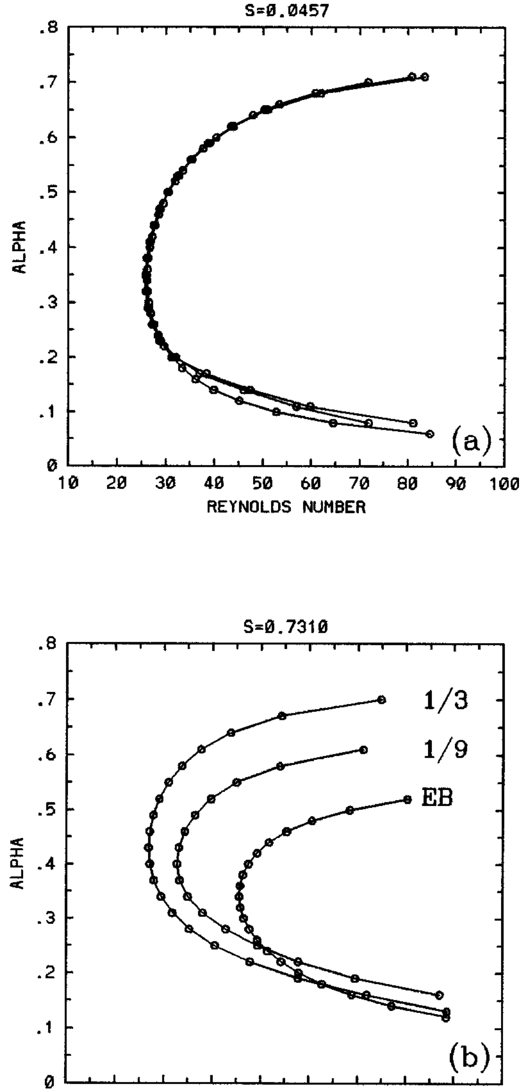

Figure 21. Marginal stability curves of the 2LQG western boundary current in an unbounded channel for $\gamma = \frac{1}{3}$, $\frac{1}{9}$ and 0 (the EB case). (a) $S = 0.0457$; note that all 3 curves collapse in one curve (b) $S = 0.7310$; note that Re_c grows when γ is reduced.

stability at moderate *Re*. This instability is a mixed barotropic-baroclinic instability becoming more barotropic (baroclinic) in the limit of large (small) deformation radius. This instability found in the meridional channel seems to be similar to the instability found in the two-layer wind-driven circulation for $\delta = 2$, but is different from the primary instabilities seen in the $\delta = 1$, 0.5 and 0.25 basins (Section 4).

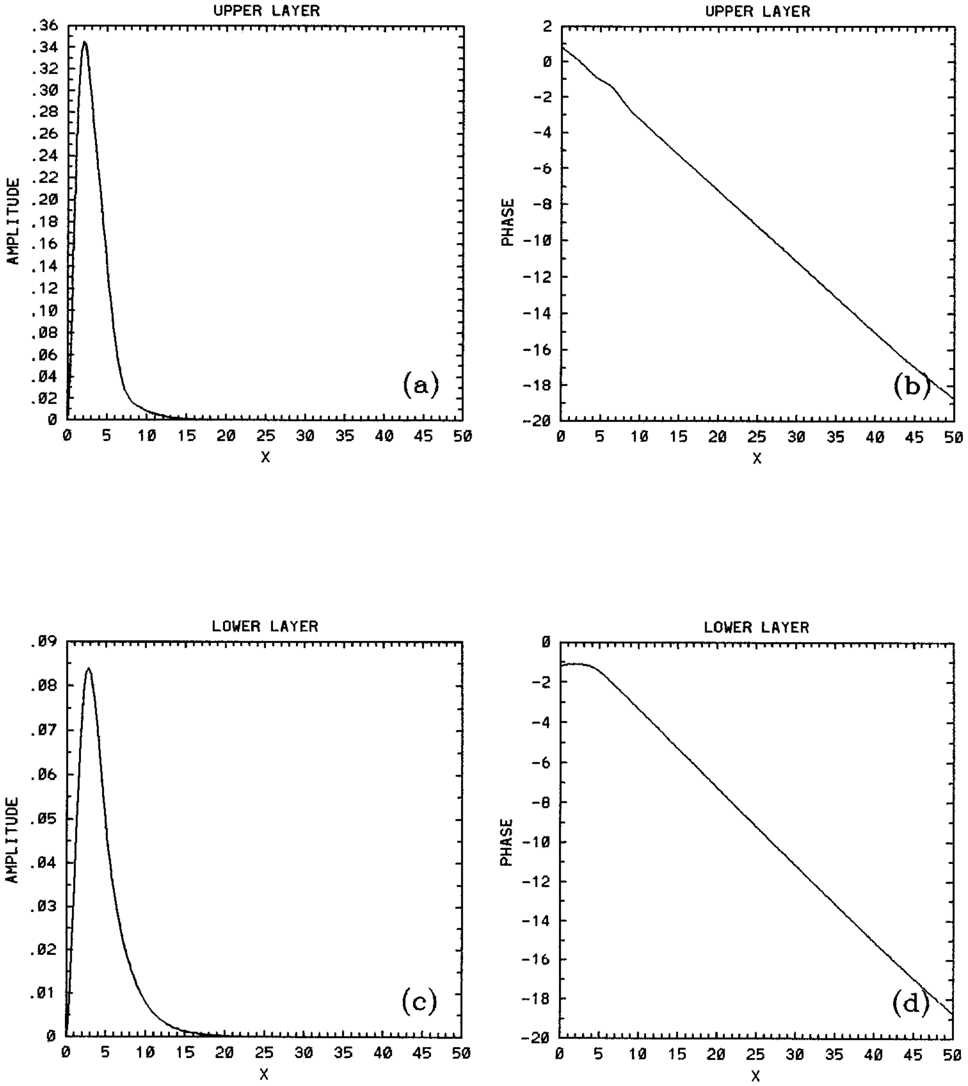

Figure 22. Amplitude and phase of the critical eigenmode $\tilde{\psi}_{1,2}(x)$ at the "nose" of the marginal curve for $S = 1.2577$ and $\gamma = 1/9$. $Re_c = 28.7$.

6. Viscous instability of vortices on an *f*-plane

In Section 4, we saw that when the western boundary current is too short, the instability of the steady, baroclinic, wind-driven circulation may be a baroclinic instability of the southwestern gyre; e.g., the $\delta = 1$ case in Section 4. The success of the comparison made in Section 5 between the channel model of a western boundary current and the instability of the $\delta = 2$ baroclinic circulation seen in Section 4 motivates us to examine the linear stability properties of an isolated, viscous baroclinic vortex with a specified azimuthal velocity, $U_1(r)$, in the upper layer. For several reasons, such a simplified model is unlikely to be a perfect model of the dynamics of the southwestern gyre seen in the steady states of the 2LQG GCM. In the 2LQG GCM, the southwestern gyre is not isolated; it is connected to western and southern boundary currents and its western and southern sides are close to rigid boundaries. In addition, there is some difficulty in choosing an appropriate profile $U_1(r)$. Nevertheless, it is interesting to look at the primary instability of an isolated viscous vortex and compare its spatial structure with the results seen in Section 4.

The stability of inviscid vortices on an *f*-plane has been extensively studied in the past (e.g., Gent and McWilliams, 1986; Flierl, 1988). Here, we introduce viscous effects. We limit ourselves to circularly symmetric vortices only weakly interacting with the basin boundaries (the radius of the basin is much larger than the characteristic radius of the vortex and the velocity decays exponentially as one approaches the wall). We exclude the β-effect because for strong vortices ($U \gg \beta_0 L$, where L is a vortex radius), which is the case here, the *f*-plane instabilities should be only weakly modified by β (Flierl, 1988).

The basic states to be considered are circularly symmetric vortices in the upper layer with no-flow in the lower layer. The basic state upper layer streamfunction is $\Psi_1(r)$ and the upper layer velocity has only an azimuthal component $U_1(r) = \partial\Psi_1(r)/\partial r$. The nondimensional, linearized equations governing the perturbations $\psi_{1,2}$ of the upper and lower layer basic states are, in cylindrical coordinates,

$$\frac{\partial}{\partial t}\left(\nabla^2\psi_1 - \frac{S}{1+\gamma}(\psi_1 - \psi_2)\right) + \frac{U_1}{r}\frac{\partial}{\partial\phi}\left(\nabla^2\psi_1 + \frac{S}{1+\gamma}\psi_2\right) - \frac{1}{r}\frac{\partial\psi_1}{\partial\phi}\frac{\partial}{\partial r}\left(\frac{1}{r}\frac{\partial}{\partial r}(rU_1)\right) = \frac{1}{Re}\nabla^4\psi_1 \tag{27a}$$

$$\frac{\partial}{\partial t}\left(\nabla^2\psi_2 - \frac{S\gamma}{1+\gamma}(\psi_2 - \psi_1)\right) - \frac{S\gamma}{1+\gamma}\frac{U_1}{r}\frac{\partial\psi_2}{\partial\phi} = \frac{1}{Re}\nabla^4\psi_2. \tag{27b}$$

The nondimensionalization is similar to that used in the channel problem, except that the velocity scale U is taken to be e times the maximum azimuthal velocity and the length scale L is the radius at which the velocity maximum is located. Since this choice for L is larger than the length scale δ_M used in the channel problem, the values of S in Section 6 will be larger than those that appeared in the channel problem of Section 5. Moreover since $UL \neq \tau_0/\rho H_1\beta_0$, the Reynolds number differs from that in Section 4. The normal mode perturbations in cylindrical coordinates are

$$\psi(r, \phi, t) = e^{im(\phi-\lambda t)}\tilde{\psi}(r) + e^{-im(\phi-\lambda^* t)}\tilde{\psi}^*(r), \tag{28}$$

where m is an azimuthal mode number. The substitution of (28) into (27a,b) yields two coupled fourth-order ODE's for $\tilde{\psi}_{1,2}$:

$$\begin{gathered}r^4\tilde{\psi}_1^{\mathrm{IV}} + 2r^3\tilde{\psi}_1''' + (-r^2(1+2m^2) - imRe\, r^3U_1)\tilde{\psi}_1'' + (r(1+2m^2) - imRe\, r^2U_1)\tilde{\psi}'_1 \\ + \left(m^2(m^2-4) + imRe\left(m^2r + \frac{S}{1+\gamma}r^3\right)U_1 + imRe\, r^3\frac{\partial Q}{\partial r}\right)\tilde{\psi}_1 - imRe\frac{S}{1+\gamma}r^3U_1\tilde{\psi}_2 \\ = -imRe\lambda\left(r^4\tilde{\psi}_1'' + r^3\tilde{\psi}'_1 - \left(m^2r^2 + \frac{S}{1+\gamma}r^4\right)\tilde{\psi}_1 + \frac{S\gamma}{1+\gamma}r^4\tilde{\psi}_2\right)\end{gathered} \tag{29a}$$

$$\begin{gathered}r^4\tilde{\psi}_2^{\mathrm{IV}} + 2r^3\tilde{\psi}_2''' - r^2(1+2m^2)\tilde{\psi}_2'' + r(1+2m^2)\tilde{\psi}'_2 \\ + \left(m^2(m^2-4) + imRe\frac{S\gamma}{1+\gamma}r^3U_1\right)\tilde{\psi}_2 \\ = -imRe\lambda\left(r^4\tilde{\psi}_2'' + r^3\tilde{\psi}_2' - \left(m^2r^2 + \frac{S\gamma}{1+\gamma}r^4\right)\tilde{\psi}_2 + \frac{S\gamma}{1+\gamma}r^4\tilde{\psi}_1\right),\end{gathered} \tag{29b}$$

where

$$\frac{\partial Q}{\partial r} = \frac{\partial}{\partial r}\left\{\frac{1}{r}\frac{\partial}{\partial r}(rU_1)\right\}$$

is the gradient of the relative vorticity of the basic state. We consider a vortex in a circular basin with the outer boundary at $r = w$. The boundary conditions at $r = 0, w$ are:

$$\tilde{\psi}_{1,2}(0) = \tilde{\psi}_{1,2}(w) = \tilde{\psi}'_{1,2}(0) = \tilde{\psi}'_{1,2}(w) = 0. \tag{30}$$

We solve the eigenvalue problem (29), (30) using the same method as in the previous sections.

Choosing a $U_1(r)$ to represent the velocity profile of the southwestern gyre is complicated by the fact that the gyre is not azimuthally symmetric about its center. We examined radial sections through the southwestern gyre in a steady solution from the GCM and found a substantial change as one moves around the gyre. In its northern and eastern sectors, away from the boundaries, the profile is qualitatively similar to

$$U_1(r) = re^{-r}, \tag{31}$$

with an azimuthal velocity profile that is an approximately linear function of r in the center of the vortex and which decays at large r. We therefore examine the stability properties of (31) below. We fix $w = 10$ which means that the core of the vortex is well separated from the walls. The far-field exponential decay gives a more crude approximation to the gyre near the western and southern walls of the basin. Our goal is to find whether the simple physical model of a viscous baroclinic vortex with azimuthal velocity (31) yields an instability mechanism, a structure of the most unstable eigenmode, and an Re_c that approximate the stability properties of the GCM. Such a physical model will provide an

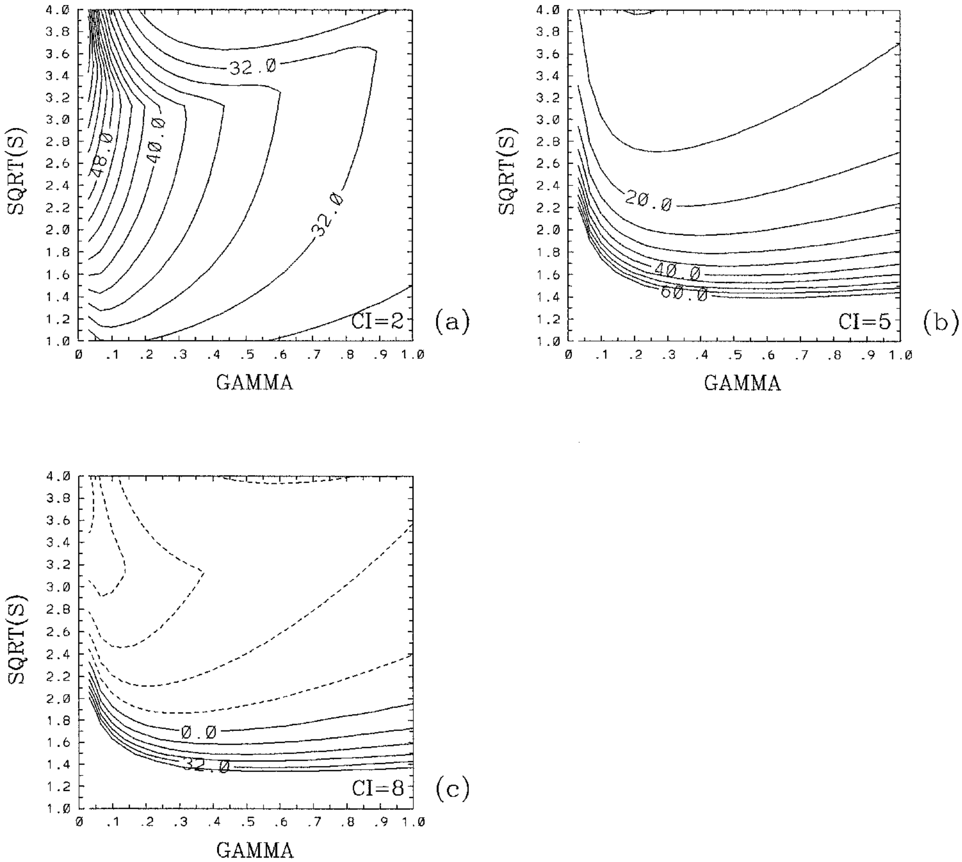

Figure 23. Marginal stability surface, Re_c, as a function of γ and $\sqrt{S}$ for a gyre with the velocity profile $U_1(r) = re^{-r}$. (a) $m = 1$; (b) $m = 2$; (c) The difference between the stability surfaces for $m = 1$ and 2 in terms of Re_c.

understanding of which processes are the most important for the kind of instability found in the GCM and which processes only modify the instability.

We found $Re_c(m, \gamma, \sqrt{S})$ for $m = 1, 2, 3$; $.05 \leq \gamma \leq 1.0$ and $0.4 \leq \sqrt{S} \leq 4.2$. The azimuthal mode with $m = 3$ is very stable with a critical Reynolds number much higher than that for $m = 1$ or 2. $Re(1, \gamma, \sqrt{S})$ and $Re(2, \gamma, \sqrt{S})$ are shown in Figure 23. The second mode becomes more stable as S is reduced (Fig. 23b). For small γ, the mode also becomes more stable as γ is reduced; for large γ it becomes more stable as γ is increased. The first eigenmode (Fig. 23a) behaves differently: for small S the mode becomes less stable if S is reduced, but for large S the stability increases as S is reduced. There is a clear boundary in the $(\gamma, \sqrt{S})$ plane separating the two regions. Crossing the boundary, the structure of the most unstable $m = 1$ eigenmode changes. The critical $m = 1$ eigenmode (Fig. 24) at $\gamma = 0.45$, $\sqrt{S} = 2.5$ spreads across the basin and interacts with the basin walls (especially in the

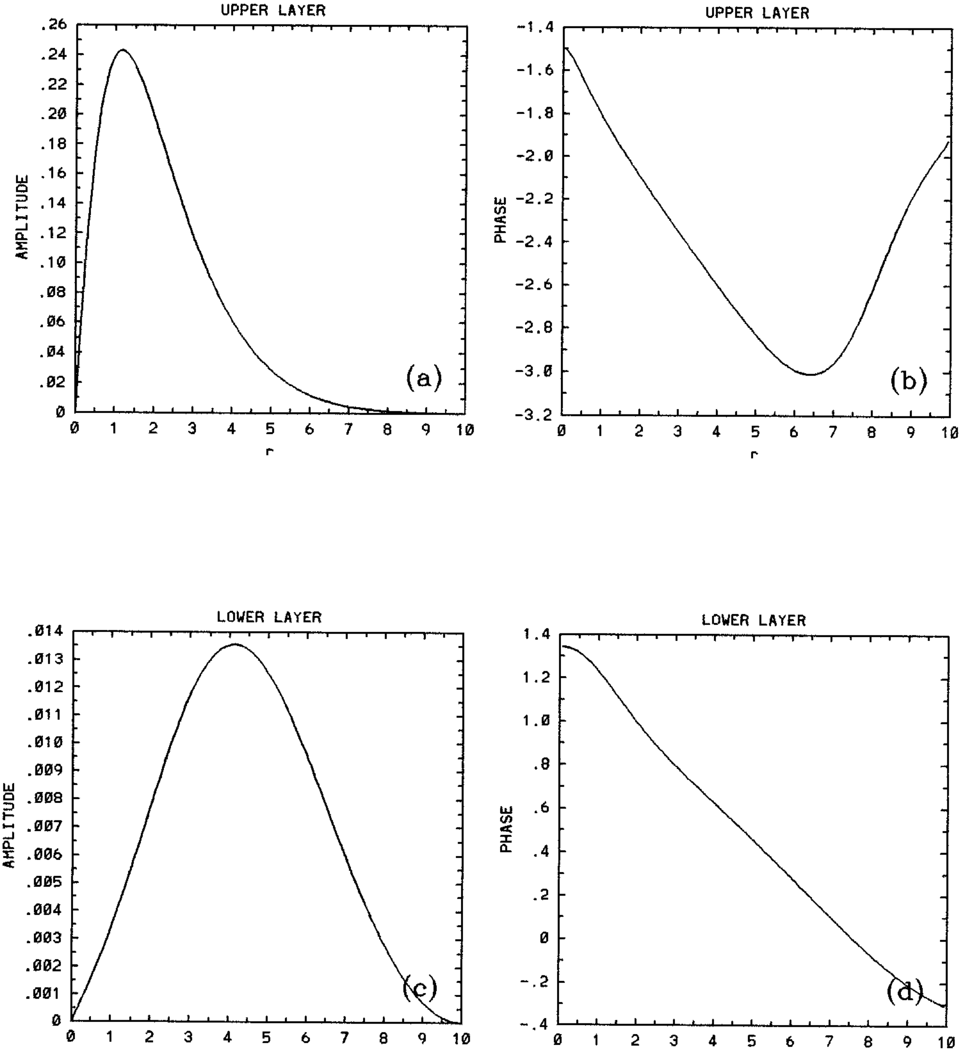

Figure 24. Amplitude and phase of the critical $m = 1$ eigenmode $\tilde{\psi}_{1,2}(x)$ at $\gamma = 0.45$, $\sqrt{S} = 2.5$.

lower layer). The phase of the eigenmode changes by an $O(1)$ amount across the basin. The critical $m = 1$ eigenmode (Fig. 25) at $\gamma = 0.45$, $\sqrt{S} = 0.4$ is trapped near the vortex core and has an oscillatory tail in the radial direction. The phase of the eigenmode changes by $O(10)$ across the basin. Our interpretation is that we are seeing two distinct eigenmodes with the same azimuthal wave number but different radial structure functions. Each has its own critical *Re* surface (marginal surface) and the two cross along the curve through the kinks in the Re_c contours (Fig. 23a). When the difference (Fig. 23c) between $Re_c(\gamma, \sqrt{S})$

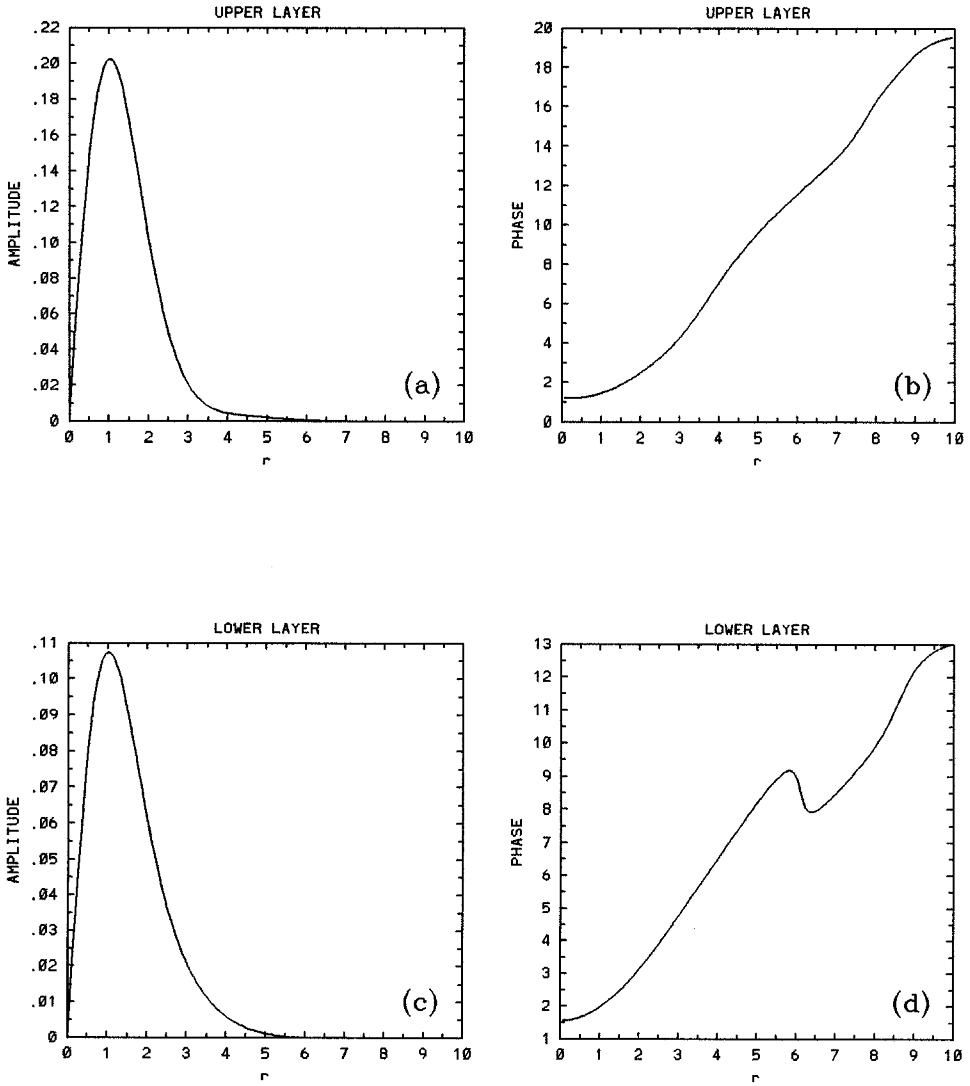

Figure 25. Amplitude and phase of the critical $m = 1$ eigenmode $\tilde{\psi}_{1,2}(x)$ at $\gamma = 0.45$, $\sqrt{S} = 4.0$. Note that the eigenmode is trapped at the vortex center and has a decaying oscillatory tail.

found for $m = 2$ and $m = 1$ is negative, the second mode is the most unstable mode. When this difference is positive, the first mode is the critical one. Figure 23c shows that $m = 1$ mode is the most unstable for smaller S while mode $m = 2$ is the most unstable for larger S; i.e., as the vortex radius becomes large in comparison to the internal deformation radius, an $m = 2$ mode becomes the dominant instability.

a. Comparison with some of the instabilities of the baroclinic GCM

In Section 4, the primary instability of the steady two-layer circulation for the case $\delta = 1$ has some of the character of a baroclinic instability of the southwestern gyre. Here, we compare that instability with the instability of the isolated vortex described above. As the first point of comparison, we compute a local critical Reynolds number of the $\delta = 1$ circulation based on the flow in the southwestern gyre and in the form used for the isolated vortex problem, i.e. $Re_c^* = eU_{max}L/\nu$, where U_{max} is the azimuthal velocity maximum (about the center of the gyre) measured in the northeast quadrant of the gyre, and L is the distance from the gyre center to the velocity maximum. Taking $L = 70$ km, $U = 20$ cm/sec and $\nu = 280$ m^2/sec, $Re_c^* \approx 136$. For the same value of γ (1/9) and $\sqrt{S}$ (3.02); i.e., $L = 70$ km, $R_d = 23.148$ km) used in Section 4, the most unstable mode of the isolated exponential vortex with velocity profile (31) is the $m = 2$ mode and the critical Reynolds number is $Re_c \approx 15.7$.

The isolated vortex is *more* unstable than the steady circulation for $\delta = 1$ in Section 4. This shows that the southwestern gyre is a plausible source of instability for the steady circulation in the $\delta = 1$ 2LQG GCM. This is reinforced by the spatial structure of the energy conversion terms associated with the instability of the circulation in the $\delta = 1$ basin.

There are several reasons why the southwestern gyre might be less unstable than our model of an isolated vortex. One is the deviation from azimuthal symmetry of the flow in the southwestern gyre. In the western and southern parts of the southwestern gyre, a sinusoidal profile of azimuthal velocity, $U_1(r) = \sin(\pi r)$, $0 \leq r \leq 1$, is a better approximation to the flow in the GCM. We examined the stability of an axisymmetric vortex with a sinusoidal azimuthal velocity profile in the upper layer and a resting lower layer in a two-layer circular basin of radius $r = 1$. Such a vortex was *more stable* than the steady circulation for $\delta = 1$ in Section 4; the critical Reynolds number was roughly 16 times larger than the critical Reynolds number of the steady circulation in the GCM. A second difference between the idealized model and the southwestern gyre is the disposition of the boundaries. The structure of the $m = 2$ eigenmode of the exponential vortex extends significantly beyond the core of the vortex (Fig. 26). We would expect such a mode to be affected by the proximity of the boundaries on the southern and western sides of the southwestern gyre. The eigenmode of the $\delta = 1$ flow in the baroclinic GCM is more strongly trapped to the southwestern gyre than the $m = 2$ mode of the exponential vortex. The periods of the marginal modes of the exponential vortex and of the critical flow in the $\delta = 1$ baroclinic GCM also differ. In the GCM, the marginal mode had a period of approximately 111 days; the marginal mode of the exponential vortex had a period of approximately 385 days.

An alternative approach would be to azimuthally average the radial profiles of azimuthal velocity in the southwestern gyre and then study the stability of an axisymmetric model constructed with the averaged radial profile. However, because of the azimuthal variation of the structure of the southwestern gyre seen in the steady states of the GCM, any axisymmetric model is unlikely to be fully realistic. Studying the stability of an axisymmet-

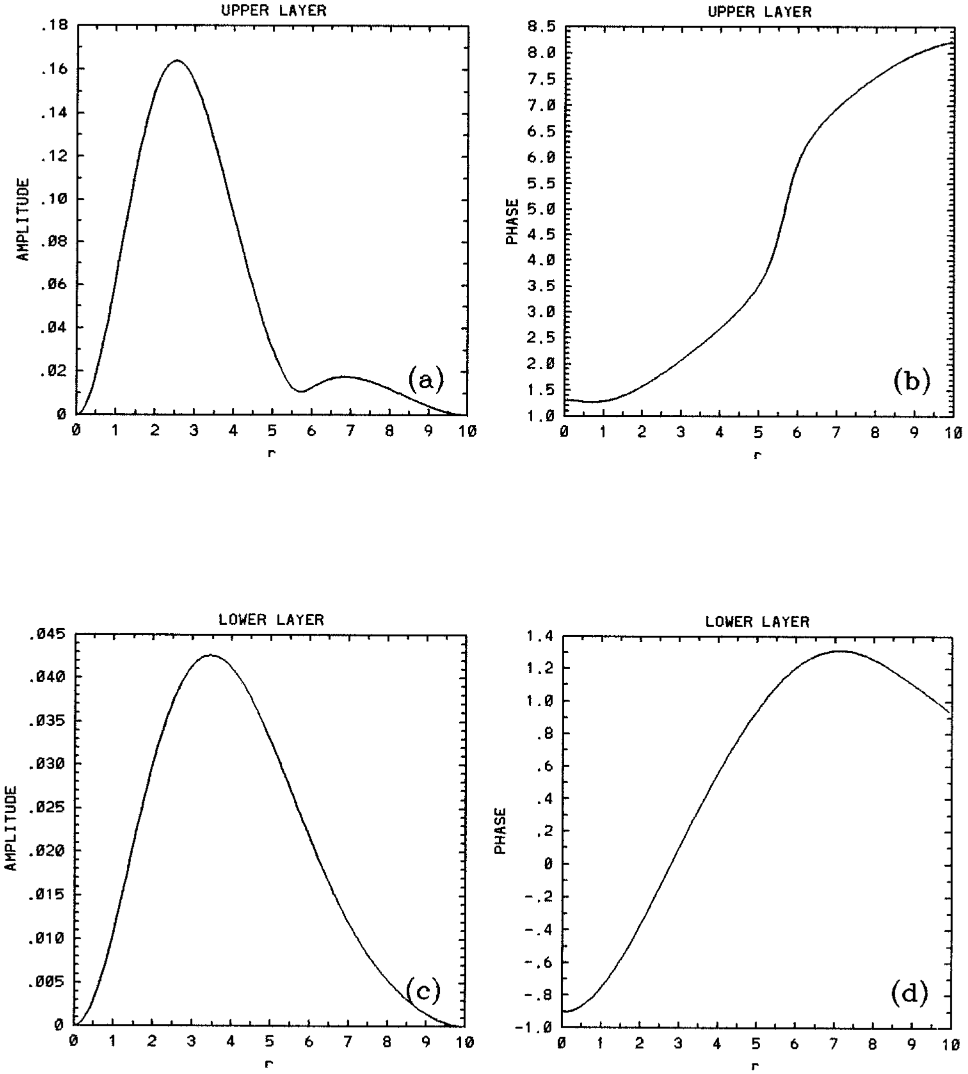

Figure 26. Amplitude and phase of the critical $m = 2$ eigenmode $\tilde{\psi}_{1,2}(x)$ at $\gamma = 1/9$, $\sqrt{S} = 3.02$.

ric vortex with an average radial profile is likely to be misleading, both because, like the process models considered above, it neglects the asymmetry and, more importantly, because the averaging process will smooth the radial gradients of potential vorticity that drive the instability.

7. Discussion and conclusions

We explored the linear stability of the steady wind-driven circulation in equivalent-barotropic (EB) and two-layer quasi-geostrophic (2LQG) models, identifying the components of the strongly asymmetric steady solutions that were responsible for the initial loss of stability of the steady flows as the Reynolds number (*Re*) was increased. The nature of the instabilities was found to be a function of the basin geometry, particularly for the baroclinic circulation.

In part, the motivation for our study came from the results of two studies of the nonlinear evolution of time-dependent single-gyre equivalent barotropic and two-layer baroclinic flows, BM1 and BM2. From these latter studies, which looked only at a single basin aspect ratio, it is clear that the structure and period of the primary linear instabilities of the steady circulations exert a strong influence on the evolution of the time-dependent circulations in the strongly nonlinear regime. In BM1 and BM2, the numerical models used, which are standard GCMs, were treated as large-dimensional dynamical systems with steady forcing and dissipation. It was shown that the behavior of these systems is strikingly low-dimensional for a wide range of control parameters including those used in modern GCMs. The low-dimensionality means that, at large times, phase space trajectories of the system asymptote to low-dimensional topological objects such as fixed points, limit cycles, tori and strange attractors. If control parameters are varied, the structure of the attractors and their stability properties change as a result of bifurcations in the system. In bifurcation sequences found in BM1 and BM2, the primary bifurcation from steady state (fixed point in the phase space) to time-dependent behavior was a super-critical Hopf bifurcation. As a result of the bifurcation, a stable limit cycle (a periodic oscillation of the flow) appeared in the system and the fixed point became unstable. It was shown that the spatio-temporal pattern associated with motion on the limit cycle was similar to that of the most unstable linear eigenmode of the unstable steady state with some modification due to nonlinearity. When control parameters were varied further from the primary bifurcation values, BM1 and BM2 found that the frequency associated with the primary bifurcation was present as a second (or third) frequency in motion on tori in phase space. Fourier spectra of chaotic motion on the strange attractors, though they contained broad band noise, also had a local maximum of power concentrated around the frequency associated with the primary bifurcation. The presence of a signal associated with the primary instability, at parameter values that are strongly supercritical relative to the marginal stability threshold, may also be seen in Jiang *et al.* (1995), Speich *et al.* (1995), Kamenkovich *et al.* (1995), Sheremet *et al.* (1995) and MB1.

Our main result has been to show that a variety of instability mechanisms may occur in the wind-driven circulation. Although the steady states of the EB and 2LQG models are the same, the critical eigenmodes and, therefore, the limit cycles are very different. This difference may result in distinct bifurcation sequences and, therefore, in distinct patterns of time-dependent behavior at low to moderate *Re*.

We found three types of instability in the EB model. One type was present in basins with meridional size equal or larger than the zonal one, but less than 2400 km. This instability was characterized by the appearance of slow oscillations with periods between 1.5 and 2 years. In this case, the spatial structure of the eigenmode was complicated; it involved several recirculations of the basic state and the standing meander in the southwestern corner of the basin. Surprisingly, we found no western boundary layer instability in these basins. A western boundary current instability was found to occur in basins of larger meridional extent ($L_y \geq 2400$ km).

We then solved the idealized stability problem of the parallel western boundary current in an unbounded meridional channel on the β-plane, extending the results obtained by Ierley and Young (1991) for the barotropic problem to the equivalent-barotropic one. This showed that the EB western boundary current is a potential source of instability at moderate Reynolds numbers in basins with sufficiently large meridional extent.

The third type of instability was present in basins with a small meridional extent and a large zonal size. This instability was localized in the standing meander between the southwestern and central gyres and was similar to the instability found in basins with $\delta < 1$ in the barotropic model of MB2. The period of this type of eigenmode was 2.6 years (the slowest oscillation found in our study).

In the 2LQG model, we found two types of instability. One type was present in basins with a sufficiently large meridional extent. This instability, a mixed barotropic-baroclinic instability, occurred in the western boundary current and was associated with the appearance of baroclinic eddies propagating southward along the western boundary. Transient eddies due to a western boundary current instability were observed by Cox (1979) in a numerical model of the Somali Current.

We solved the idealized stability problem of a two-layer quasi-geostrophic western boundary current in an unbounded meridional channel on the β-plane and showed that the idealized instability is rather similar to the instability found in the 2LQG GCM with aspect ratio $\delta = 2$. In the GCM, the boundary current instability was modified by the presence of zonal walls and the western recirculation. The oscillations appearing at the onset of instability had a period of 105 days.

A second type of instability was present in basins of smaller meridional extent. This instability was also seen in BM2. It occurs in a large part of the southwestern recirculation gyre and is essentially baroclinic. In the case of $\delta = 0.25$ (a large zonal extent), baroclinic instability occurred not only in the gyre but also in the westward return flow adjacent to the gyre. The periods at the onset of the instability were 111 days for $\delta = 1$, 120 days for $\delta = 0.5$ (results of BM2) and 102 days for $\delta = 0.25$.

Only in the EB model did we find a primary instability that was an oscillation with an interannual time scale. In contrast, the 2LQG model exhibited oscillation periods ranging between 3.4 and 4 months.

Acknowledgments. This work was supported by the National Science Foundation (grant OCE-9301318). The authors wish to thank Drs. G. Ierley, V. Sheremet and P. Cessi for several interesting discussions on the wind-driven circulation.

APPENDIX A

Brief description of the numerical model

The numerical model solves (2) and (3) (or (6) and (7) in the EB limit) with the boundary conditions (4) and the mass conservation constraint (5) in dimensional form. The equations are discretized with second order finite differences and advanced in time with a leapfrog scheme. The computational mode of the leapfrog instability is damped by a three-point (0.03-0.94-0.03) time smoother applied to $\zeta_{1,2}$ (Asselin, 1972). The Jacobian is discretized following Arakawa (1966) and does not generate energy. The elliptical problem (3) (or (7) in the EB limit) is solved using a FACR method (Hockney, 1970). The numerical model is similar to the one used by Holland (1978). The horizontal resolution is 6.25 km, and the grid points are equally spaced in x and y.

a. Techniques for finding steady states and unstable normal modes

The primary stability threshold is found by using the evolutionary model just described. The approach is based on the idea that a change in the stability properties of a steady solution will lead to a change in the nature of the solution to which the model asymptotes at large time (e.g. Glendinning, 1994). Examples of such changes are from a steady state to a limit cycle (a Hopf bifurcation) or from a single possible steady state to multiple possible steady states. Since both the mathematical model described by (2) and (3) and typical numerical ocean GCMs are examples of dynamical systems, the general theory of such systems immediately tells us what we should expect to see. Since there is no spatial symmetry in the problem, the generic type of change in number of steady states is a saddle-node bifurcation. In general, the occurrence of a nearby saddle-node bifurcation does not immediately change the stability properties of a solution on a branch of steady states that exists on both sides of the saddle-node bifurcation. Therefore if a steady state changes from being stable to being unstable as ν is decreased, we expect the instability that sets in to be an oscillatory instability. Two possibilities then arise: close to the stability threshold, but on its unstable side, the oscillatory instability will either equilibrate to a periodic solution with small amplitude that lies close to the steady state—a *supercritical* Hopf bifurcation, or it will wander far from the unstable steady state—a characteristic of a *subcritical* Hopf bifurcation.

Starting with a relatively large value of ν, the numerical model of (2) and (3) quickly asymptotes to a steady state. This state is then used as the initial condition for a run at a smaller value of ν. This procedure is repeated until we reach a value of ν for which the numerical model fails to converge to a steady state. Instead we find that the solution settles down to a limit cycle. Using an instantaneous state from the limit cycle as an initial condition, we were able to increase ν slightly and obtain a limit cycle of smaller amplitude. Working from limit cycles to large values of ν and from stable steady states to smaller values of ν, we were able to bracket the stability boundary. For the parameter values that we used, we found only supercritical Hopf bifurcations (the amplitudes of the limit cycles tended to zero as the stability boundary was approached from the unstable side) although in

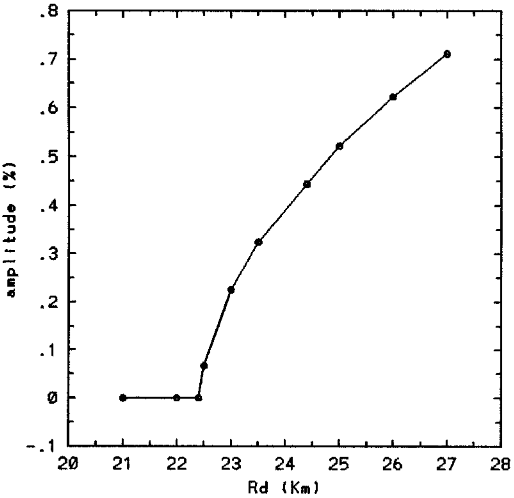

Figure 27. The relative energy oscillation of the EB circulation with $\delta = 0.5$ and $\nu = 102$ m^2/sec as a function of R_d.

the case of a homogeneous ocean, there are some parameter values at which the primary bifurcation is a subcritical Hopf bifurcation.

We obtain the structure of the linear eigenmode corresponding to the primary instability as follows. After bracketing the marginal value of ν, ν_c say, we pick a value of ν slightly below ν_c and then we compute the *unstable* steady state using one of the following two methods.

The first, and more efficient method is based on the fact that variation of R_d does not change the steady state governed by (8), but influences its stability properties. In the 2LQG situation this is true for variation of H_2 as well. Empirically, we found that reduction of R_d often stabilizes the flow. This is illustrated by Figure 27 where the relative amplitude (in terms of total energy fluctuations) of the EB limit cycle at $\delta = 0.5$ and $\nu = 102$ m^2/sec is shown as a function of R_d. Changing R_d from its standard value of 24.4 km to a value less than 22.4 km makes the steady state linearly stable. In the two-layer case the stabilization may be achieved by reducing R_d and increasing H_2. The stabilizing effect of such parameter variations is not limited to idealized western boundary currents and f-plane vortices (Sections 5 and 6), but is present for most of our general circulation solutions.

The second method (BM1) was used when the first one did not work. A slightly supercritical limit cycle was computed, and a periodic solution was averaged over one period. The time-averaged state was used as an initial condition, the model was integrated in time, and the solution was averaged again. We iterated this procedure until the solution converged to the unstable steady state. The method is robust provided that the bifurcation is supercritical and iterations start sufficiently close to the critical threshold.

After computing the unstable steady state for a slightly supercritical ν, we use an iterative procedure (BM1) for extracting the most unstable growing linear eigenmode. We first constructed a version of the EB and 2LQG models linearized about a general, steady basic state. The unstable streamfunction and vorticity fields of a weakly unstable steady state, found by the techniques discussed in the preceding paragraphs, were used for the basic state of the linear model. The linear model was then initialized with a small amplitude perturbation derived by taking the difference between the approximation to the unstable steady state and a nearby weakly time-dependent state. This difference field was obtained as a by-product of the search for the steady state and can safely be assumed to include a projection on the unstable normal mode. The linear model was integrated over a finite period of time, chosen to be comparable to one or two *e*-folding periods, and the perturbation grew in amplitude. At the end of the integration interval, the perturbation was rescaled to its initial (smaller) amplitude and the cycle was repeated. After several iterations the perturbation approximates the dominant eigenmode. (The same approach works at a slightly subcritical value of ν except that at the end of each integration the rescaling of the perturbation back to its initial amplitude is a magnification since the dominant eigenmode is decaying.)

b. Solving for the eigenmodes of the Munk boundary layer profiles

The eigenvalue problem (19) was discretized using second-order finite differences to represent the derivatives and solved using the QR algorithm (Press *et al.,* 1992). Choosing finite differences for the stability analysis of the idealized western boundary currents and vortices, we make the stability problems consistent with the GCMs.

The eigenvalue problem solver was tested on plane Poiseuille flow (Orszag, 1971) with the side walls at $x = -1$ and $+1$. The Poiseuille flow eigenvalue for $\alpha = 1$ and $Re = 10000$ is $0.23752649 + 0.00373967i$ (Orszag, 1971). We computed this eigenvalue with successively increasing resolution on the interval $(-1, +1)$:

100 points: $0.2354 + 0.00314i$

150 points: $0.2365 + 0.00354i$

200 points: $0.2370 + 0.00364i$

250 points: $0.2372 + 0.00368i$.

This test shows that the finite difference scheme and the eigenvalue solver work satisfactorily and that there is convergence toward the value found in Orszag (1971). One caveat is that the plane Poiseuille flow is much smoother than the Munk boundary layer profile. In our calculations we used a mesh with 200 points.

APPENDIX B

One of the tools that proved useful for diagnosing the properties of slowly growing eigenmodes of weakly unstable steady circulations in the EB and 2LQG models was an analysis of the spatial structure of the rates at which energy is transferred between the steady state and the eigenmode. The conversion term for the EB model is derived below; the baroclinic and barotropic conversion terms for the 2LQG model are derived in Appendix C.

Since our primary bifurcations are supercritical Hopf bifurcations, close to the stability threshold, the eigenvalue of the unstable mode has a period that is $O(1)$ and a growth rate that is small. We take advantage of this separation of timescales, introducing an averaging time equal to one period of the perturbation, a fast time, $t' = t$, and a slow time variable, t_0, with which to represent variations on time scales long compared to the period, T, of the eigenmode. We decompose the time-dependent streamfunction into a slowly varying mean state $\Psi_1(x, y, t_0) = \langle \psi_1(x, y, t) \rangle$ and a rapidly varying perturbation $\psi_1'(x, y, t', t_0) = \psi_1 - \Psi_1$, where $\langle * \rangle$ is the averaging operator defined by (11); thus

$$\psi_1(x, y, t) = \Psi_1(x, y, t_0) + \psi_1'(x, y, t', t_0).$$

The kinetic and potential energy densities of the EB flow are

$$K(x, y, t) = \frac{|\nabla \psi_1(x, y, t)|^2}{2}; \quad \Pi(x, y, t) = S\frac{\psi_1^2(x, y, t)}{2}.$$

Multiplying (6) by Ψ_1, taking a time-average, $\langle * \rangle$, over one period, and making use of the fact that $\langle \psi_1'(x, y, t) \rangle = 0$, we get, after some rearrangement, an equation for the energy density $E = |\nabla \Psi_1|^2/2 + S(\Psi_1^2)/2$ of the mean state:

$$\frac{\partial E}{\partial t_0} = \nabla \cdot \mathbf{M} - P + F + D, \tag{B.1}$$

where

$$\begin{aligned}
\mathbf{M} = {} & \mathbf{i}\varepsilon\left\{\frac{\Psi_1^2}{2}\nabla^2\Psi_{1y} - \Psi_1\langle \psi'_{1y}\nabla^2\psi'_1\rangle + \Psi_{1x}\langle \psi'_{1x}\psi'_{1y}\rangle - \frac{\Psi_{1y}}{2}\langle \psi'^2_{1x} - \psi_{1y}'^2\rangle + \frac{\Psi_1^2}{2\varepsilon}\right\} \\
& - \mathbf{j}\varepsilon\left\{\frac{\Psi_1^2}{2}\nabla^2\Psi_{1x} - \Psi_1\langle \psi'_{1x}\nabla^2\psi'_1\rangle + \Psi_{1y}\langle \psi'_{1x}\psi'_{1y}\rangle + \frac{\Psi_{1x}}{2}\langle \psi'^2_{1x} - \psi'^2_{1y}\rangle\right\} \\
& + \mu(\nabla\Psi_1 \cdot \nabla\nabla\Psi_1 - \Psi_1\nabla\nabla^2\Psi_1) + \Psi_1\nabla\Psi_{1t_0} \\
P = {} & -\varepsilon\langle \psi_{1x}'J(\psi_1', \Psi_{1x}) + \psi_{1y}'J(\psi_1', \Psi_{1y})\rangle \\
F = {} & -\Psi_1\nabla \times \tau \\
D = {} & -\mu|\nabla\nabla\Psi_1|^2
\end{aligned} \tag{B.2}$$

$\mathbf{M}$ is a flux of mean energy, F is the rate of direct forcing of the mean by the wind stress, and D is the rate of diffusive dissipation of mean energy. Multiplying (6) by ψ'_1, taking the time-average over one period and rearranging terms we get an equation for the evolution of the perturbation energy density $\langle E'\rangle = \langle|\nabla\psi'_1|^2/2\rangle + S\langle\psi_1'^2/2\rangle$

$$\frac{\partial\langle E'\rangle}{\partial t_0} = \langle\nabla\cdot\mathbf{m}\rangle + P + d, \tag{B.3}$$

where

$$\begin{aligned}
\mathbf{m} = {}& \psi'_1\nabla\psi'_{1t} \\
& + \mathbf{i}\varepsilon\left\{\frac{\psi_1'^2}{2}\nabla^2(\Psi_1+\psi'_1)_y - \Psi_{1y}\psi'_1\nabla^2\psi'_1 - \Psi_{1x}\psi'_{1x}\psi'_{1y} + \frac{\Psi_{1y}}{2}(\psi_{1x}'^2 - \psi_{1y}'^2) + \frac{\psi_1'^2}{2\varepsilon}\right\} \\
& - \mathbf{j}\varepsilon\left\{\frac{\psi_1'^2}{2}\nabla^2(\Psi_1+\psi'_1)_x - \Psi_{1x}\psi'_1\nabla^2\psi'_1 - \Psi_{1y}\psi'_{1x}\psi'_{1y} - \frac{\Psi_{1x}}{2}(\psi_{1x}'^2 - \psi_{1y}'^2)\right\} \qquad \text{(B.4)} \\
& + \mu(\nabla\psi'_1\cdot\nabla\nabla\psi'_1 - \psi'_1\nabla\nabla^2\psi'_1) \\
d = {}& -\mu\langle|\nabla\nabla\psi'_1|^2\rangle
\end{aligned}$$

m is a perturbation energy flux and d is the rate of diffusive dissipation of perturbation energy. P enters both (B.1) and (B.3) with different signs and represents an energy exchange between the mean state and the perturbation. Since we are looking at energy conversion in the approximately linear limit close to the stability threshold, we can use the basic state as an approximation to the mean over a period when evaluating P.

APPENDIX C

The energy equations for the 2LQG flow can be derived using an approach similar to that in Appendix B. Again our primary bifurcations are supercritical Hopf bifurcations, so that close to the stability threshold, the eigenvalue of the unstable mode has a period that is $O(1)$ and a growth rate that is small, allowing us to split the time-dependent streamfunctions $\psi_{1,2}$ into a slowly varying mean state $\Psi_{1,2}(x, y, t_0)$ and rapidly varying perturbations $\psi'_{1,2}(x, y, t', t_0)$. Thus, the full streamfunction is

$$\psi_{1,2}(x, y, t) = \Psi_{1,2}(x, y, t_0) + \psi'_{1,2}(x, y, t', t_0).$$

After substituting this expression into the equations of motion (2.1 and 2.2), we multiply Eq. (2.1) by $-\Psi_1(H_1/H)$ and Eq. (2.2) by $-\Psi_2(H_2/H)$, then add the resulting equations together and take a time-average as defined in (11). The energy density of the mean state is

$$E(x, y) = \sum_{i=1,2}\frac{H_i}{H}\frac{|\nabla\Psi_i|^2}{2} + \frac{S\gamma}{2(1+\gamma)^2}(\Psi_2 - \Psi_1)^2, \tag{C.1}$$

and

$$\partial E/\partial t_0 = \nabla\cdot\mathbf{M} - P - R + F + D. \tag{C.2}$$

The flux term in (C.2) is

$$\begin{aligned}
\mathbf{M} = +\mathbf{i}\varepsilon\bigg\{ & \frac{H_1}{H}\frac{\Psi_1^2}{2}\left(\nabla^2\Psi_{1y} + \frac{S}{1+\gamma}\Psi_{2y}\right) + \frac{H_2}{H}\frac{\Psi_2^2}{2}\left(\nabla^2\Psi_{2y} + \frac{S\gamma}{1+\gamma}\Psi_{1y}\right) \\
& + \sum_{i=1,2}\frac{H_i}{H}\left(-\Psi_i\langle\psi'_{iy}\nabla^2\psi'_i\rangle + \Psi_{ix}\langle\psi'_{ix}\psi'_{iy}\rangle - \Psi_{iy}\left\langle\frac{\psi'^2_{ix} - \psi'^2_{iy}}{2}\right\rangle\right) \\
& + \frac{S\gamma}{2(1+\gamma)^2}(\Psi_1 - \Psi_2)\langle(\psi'_1 - \psi'_2)(\psi'_1 + \psi'_2)_y\rangle + \sum_{i=1,2}\frac{H_i}{\varepsilon H}\frac{\Psi_i^2}{2}\bigg\} \\
- \mathbf{j}\varepsilon\bigg\{ & \frac{H_1}{H}\frac{\Psi_1^2}{2}\left(\nabla^2\Psi_{1x} + \frac{S}{1+\gamma}\Psi_{2x}\right) + \frac{H_2}{H}\frac{\Psi_2^2}{2}\left(\nabla^2\Psi_{2x} + \frac{S\gamma}{1+\gamma}\Psi_{1x}\right) \\
& - \sum_{i=1,2}\frac{H_i}{H}\left(\Psi_i\langle\psi'_{ix}\nabla^2\psi'_i\rangle - \Psi_{iy}\langle\psi'_{ix}\psi'_{iy}\rangle - \Psi_{ix}\left\langle\frac{\psi'^2_{ix} - \psi'^2_{iy}}{2}\right\rangle\right) \\
& + \frac{S\gamma}{2(1+\gamma)^2}(\Psi_1 - \Psi_2)\langle(\psi'_1 - \psi'_2)(\psi'_1 + \psi'_2)_x\rangle\bigg\} \\
& + \mu\sum_{i=1,2}\frac{H_i}{H}(\nabla\Psi_i \cdot \nabla\nabla\Psi_i - \Psi_i\nabla\nabla^2\Psi_i) + \sum_{i=1,2}\frac{H_i}{H}\Psi_i\nabla\Psi_{it_0}.
\end{aligned}$$

The energy exchange terms between the mean state and the perturbations are

$$\begin{aligned}
P &= -\varepsilon\sum_{i=1,2}\frac{H_i}{H}\langle\psi'_{ix}J(\psi'_i, \Psi_{ix}) + \psi'_{iy}J(\psi'_i, \Psi_{iy})\rangle \\
R &= -\varepsilon\frac{S\gamma}{(1+\gamma)^2}\left\langle(\psi'_1 - \psi'_2)J\left(\frac{1}{2}[\psi'_1 + \psi'_2], \Psi_1 - \Psi_2\right)\right\rangle
\end{aligned} \tag{C.3}$$

where the first term P is the energy exchange between the mean state and the perturbations due to work done by Reynolds stresses. The second term R represents the energy exchange associated with a divergent eddy heat flux. The rate of direct forcing of the mean by the wind stress F and the rate of diffusive dissipation of mean energy in (C.2) are

$$F = -\frac{H_1}{H}\Psi_1\nabla \times \tau$$

$$D = -\mu\sum_{i=1,2}\frac{H_i}{H}(\nabla\nabla\Psi_i : \nabla\nabla\Psi_i)$$

The perturbation energy density of the system is

$$\langle E' \rangle = \sum_{i=1,2} \frac{H_i}{H} \left\langle \frac{|\nabla \psi_i|^2}{2} \right\rangle + \frac{S\gamma}{2(1+\gamma)^2} \langle (\psi'_2 - \psi'_1)^2 \rangle. \tag{C.4}$$

If we multiply (2.1) by $-(H_1/H)\psi'_1$ and (2.2) by $-(H_2/H)\psi'_2$, and time-average, we obtain

$$\frac{\partial \langle E' \rangle}{\partial t_0} = \langle \nabla \cdot \mathbf{m} \rangle + P + R + d, \tag{C.5}$$

The expression for the flux **m** is

$$\begin{aligned}
\mathbf{m} = {} & \sum_{i=1,2} \frac{H_i}{H} \psi'_i \nabla \frac{\partial \psi'_i}{\partial t} + \mathbf{i}\varepsilon \Bigg\{ \sum_{i=1,2} \frac{H_i}{H} \frac{\psi_i'^2}{2} \nabla^2 (\Psi_i + \psi'_i)_y \\
& + \sum_{i=1,2} \frac{H_i}{H} \left[-\psi'_i \Psi_{iy} \nabla^2 \psi'_i - \psi'_{ix} \psi'_{iy} \Psi_{ix} + \frac{\psi_{ix}'^2 - \psi_{iy}'^2}{2} \Psi_{iy} \right] \\
& + \frac{S\gamma}{(1+\gamma)^2} \left[\frac{\psi_1'^2}{2} (\Psi_2 + \psi'_2)_y + \frac{\psi_2'^2}{2} (\Psi_1 + \psi'_1)_y \right] \\
& + \frac{S\gamma}{2(1+\gamma)^2} \left[\frac{1}{2} (\Psi_1 - \Psi_2)_y (\psi'_1 - \psi'_2)(\psi'_1 + \psi'_2) - \psi'_1 \psi'_2 (\Psi_1 + \Psi_2)_y \right] + \sum_{i=1,2} \frac{H_i}{\varepsilon H} \frac{\psi_i'^2}{2} \Bigg\} \\
& - \mathbf{j}\varepsilon \Bigg\{ \sum_{i=1,2} \frac{H_i}{H} \frac{\psi_i'^2}{2} \nabla^2 (\Psi_i + \psi'_i)_x + \sum_{i=1,2} \frac{H_i}{H} \left[-\psi'_i \Psi_{ix} \nabla^2 \psi'_i - \psi'_{ix} \psi'_{iy} \Psi_{iy} - \frac{\psi_{ix}'^2 - \psi_{iy}'^2}{2} \Psi_{ix} \right] \\
& + \frac{S\gamma}{(1+\gamma)^2} \left[\frac{\psi_1'^2}{2} (\Psi_2 + \psi'_2)_x + \frac{\psi_2'^2}{2} (\Psi_1 + \psi'_1)_x \right] \\
& + \frac{S\gamma}{2(1+\gamma)^2} \left[\frac{1}{2} (\Psi_1 - \Psi_2)_x (\psi'_1 - \psi'_2)(\psi'_1 + \psi'_2) - \psi'_1 \psi'_2 (\Psi_1 + \Psi_2)_x \right] \Bigg\} \\
& + \mu \sum_{i=1,2} \frac{H_i}{H} (\nabla \psi'_i \cdot \nabla \nabla \psi'_i - \psi'_i \nabla \nabla^2 \psi'_i)
\end{aligned}$$

and the rate of diffusive dissipation of perturbation energy is

$$d = -\mu \sum_{i=1,2} \frac{H_i}{H} \langle \nabla \nabla \psi'_i : \nabla \nabla \psi'_i \rangle$$

In those regions of the circulation where the sum of the exchange terms, $P + R$, is positive, perturbations gain energy from the slowly varying mean state.

REFERENCES

Arakawa, A. 1966. Computational design for long-term integration of the equations of fluid motions. J. Comp. Phys., *1,* 119–143.

Asselin, R. 1972. Frequency filter for time integrations. Mon. Wea. Rev., *100,* 487–490.

Berloff, P. and J. McWilliams. 1998. Large-scale, low-frequency variability in wind-driven ocean gyres. J. Phys. Oceanogr. (submitted).

Berloff, P. and S. P. Meacham. 1997. The dynamics of an equivalent-barotropic model of the wind-driven circulation. J. Mar. Res., *55,* 523–563.

—— 1998. The dynamics of a simple baroclinic model of the wind-driven circulation. J. Phys. Oceanogr., *28,* 361–388.

Bjerknes, J. 1964. Atlantic air-sea interaction. Adv. Geophys., *10,* 1–82.

Bryan, K. 1963. A numerical investigation of a nonlinear model of a wind-driven ocean. J. Atmos. Sci., *20,* 594–606.

—— 1969. A numerical method for the study of the circulation of the World Ocean. J. Comp. Phys., *4,* 347–376.

Cessi, P. and G. Ierley. 1995. Symmetry-breaking multiple equilibria in quasi-geostrophic wind-driven flows. J. Phys. Oceanogr., *25,* 1196–1205.

Cox, M. D. 1979. A numerical study of Somali Current eddies. J. Phys. Oceanogr., *9,* 311–326.

—— 1987. An eddy-resolving model of the ventilated thermocline: time dependence. J. Phys. Oceanogr., *17,* 1044–1056.

Dickinson R. and F. Clare. 1973. Numerical study of the unstable modes of a hyperbolic-tangent barotropic shear flow. J. Atmos. Sci., *30,* 1035–1049.

Dijkstra, H. A. and C. A. Katsman. 1997. Temporal variability of the wind-driven quasi-geostrophic double gyre ocean circulation: basic bifurcation diagrams. Geophys. Astrophys. Fluid Dyn., *85,* 195–232.

Drazin, P. 1992. Nonlinear Systems, Cambridge University Press, Cambridge, 317 pp.

Flierl, G. 1988. On the instability of geostrophic vortices. J. Fluid Mech., *197,* 349–388.

Frankignoul, C. 1995. Climate spectra and stochastic climate models, *in* Analysis of Climate Variability. Application of Statistical Techniques, H. von Storch and A. Navarra, eds., Springer-Verlag, Berlin, 29–51.

Gent, P. and J. C. McWilliams. 1986. The instability of circular vortices. Geophys. Astrophys. Fluid Dyn., *35,* 209–233.

Glendinning, P. 1994. Stability, Instability, and Chaos: An Introduction to the Theory of Nonlinear Differential Equations, Cambridge Univ. Press, Cambridge, 388 pp.

Goodman, J. and J. C. Marshall. 1998. A model of decadal, middle-latitude, atmosphere-ocean coupled modes. J. Climate, (in press).

Hasselman, K. 1976. Stochastic climate models. Part I: Theory. Tellus, *28,* 473–485.

Helfrich, K. and U. Send. 1988. Finite-amplitude evolution of two-layer geostrophic vortices. J. Fluid Mech., *197,* 331–348.

Hockney, R. 1970. The potential calculation and some applications. Methods in Comput. Phys., *9,* 136–211.

Holland, W. 1978. The role of mesoscale eddies in the general circulation of the ocean—Numerical experiments using a wind-driven quasigeostrophic model. J. Phys. Oceanogr., *8,* 363–392.

Holland, W. and L. Lin. 1975a. On the generation of mesoscale eddies and their contribution to the oceanic general circulation. I. A preliminary numerical experiment. J. Phys. Oceanogr., *5,* 642–657.

—— 1975b. On the generation of mesoscale eddies and their contribution to the oceanic general circulation. II. A parameter study. J. Phys. Oceanogr., *5,* 658–669.

Howard, L. and P. Drazin. 1964. On instability of parallel flow of inviscid fluid in a rotating system with variable Coriolis parameter. J. Math. and Phys., *43,* 83–99.

Ierley, G. R. and V. Sheremet. 1995. Multiple solutions and advection-dominated flows in the wind-driven circulation. Part I: Slip. J. Mar. Res., *53,* 703–737.

Ierley, G. R. and W. R. Young. 1991. Viscous instabilities in the western boundary layer. J. Phys. Oceanogr., *21,* 1323–1332.

Jiang, S., F. Jin and M. Ghil. 1995. Multiple equilibria, periodic, and aperiodic solutions in a wind-driven, double-gyre, shallow-water model. J. Phys. Oceanogr., *25,* 764–786.

Kamenkovich, V., V. Sheremet, A. Pastushkov and S. Belotserkovsky. 1995. Analysis of the barotropic model of the subtropical gyre in the ocean for finite Reynolds numbers. Part I. J. Mar. Res., *53,* 959–994.

Latif, M. and T. Barnett. 1994. Causes of decadal climate variability over the North Pacific and North America. Science, *266,* 634–637.

—— 1996. Decadal climate variability over the North Pacific and North America: Dynamics and predictability. J. Climate, *9,* 2407–2423.

LeProvost, C. and J. Verron. 1987. Wind-driven ocean circulation transition to barotropic instability. Dyn. Atmos. Oceans, *11,* 175–201.

Meacham, S. P. 1998a. Low frequency variability in the wind-driven circulation. J. Phys. Oceanogr., (submitted).

—— 1998b. Decadal variability in the wind-driven circulation (In preparation).

Meacham, S. P. and P. Berloff. 1997a. Barotropic, wind-driven circulation in a small basin. J. Mar. Res., *55,* 407–451.

—— 1997b. Instabilities of a steady, barotropic, wind-driven circulation. J. Mar. Res., *55,* 885–913.

Moro, B. 1990. On the nonlinear Munk model. II: Stability. Dyn. Atmos. Oceans, *14,* 203–227.

Munk, W. 1950. On the wind-driven ocean circulation. J. Meteorol., *7,* 79–93.

Nakamura, M., P. H. Stone and J. Marotzke. 1994. Destabilisation of the thermohaline circulation by atmospheric eddy transports. J. Climate, *7,* 1870–1882.

Namias, J. 1959. Recent seasonal interactions between the North Pacific waters and the overlying atmospheric circulation. J. Geophys. Res., *64,* 631–646.

—— 1969. Seasonal interactions between the North Pacific and the atmosphere during the 1960s. Mon. Wea. Rev., *97,* 173–192.

Orszag, S. 1971. Accurate solution of the Orr-Sommerfeld stability equation. J. Fluid Mech., *50,* 689–703.

Packard, N., J. Crutchfield, J. Farmer and R. Shaw. 1980. Geometry from a time series. Phys. Rev. Lett., *45,* 712–716.

Pedlosky, J. 1987. Geophysical Fluid Dynamics, 2nd edition, Springer-Verlag, NY, 710 pp.

—— 1970. Finite-amplitude baroclinic waves. J. Atmos. Sci., *27,* 15–30.

Press, W., S. Teukolsky, W. Vetterling, and B. Flannery. 1992. Numerical Recipes in Fortran: The Art of Scientific Computing. 2nd edition, Cambridge University Press, 963 pp.

Santer, B. D., U. Mikolajewicz, W. Bruggemann, U. Cubasch, K. Hasselmann, H. Hock, E. Maier-Reimer and T. M. L. Wigley. 1995. Ocean variability and its influence on the detectability of greenhouse warming signals. J. Geophys. Res., *100,* 10693–10725.

Sheremet, V., G. R. Ierley and V. Kamenkovich. 1997. Eigenanalysis of the two-dimensional wind-driven ocean circulation problem. J. Mar. Res., *55,* 57–92.

Sheremet, V., V. Kamenkovich and A. Pastushkov. 1995. Analysis of the barotropic model of the subtropical gyre in the ocean for finite Reynolds numbers. Part II. J. Mar. Res., *53,* 995–1024.

Spall, M. A. 1996. Dynamics of the Gulf Stream/Deep Western Boundary Current Crossover. Part I: Entrainment and recirculation. J. Phys. Oceanogr., *26,* 2152–2168.

Speich, S., H. Dijkstra and M. Ghil. 1995. Successive bifurcations in a shallow-water model applied to the wind-driven ocean circulation. Nonlin. Proc. Geophys., *2,* 241–268.

Stommel, H. 1948. The westward intensification of wind-driven oceanic currents. Trans. Am. Geophys. Union, *29,* 202–206.

—— 1961. Thermohaline convection with two stable regimes of flow. Tellus, *13,* 224–230.

Talley, L. 1983a. Radiating barotropic instability. J. Phys. Oceanogr., *13,* 972–987.

—— 1983b. Radiating instabilities of thin baroclinic jets. J. Phys. Oceanogr., *13,* 2161–2181.

Wunsch, C. 1992. Decade-to-century changes in the ocean circulation. Oceanography, *5,* 99–106.

Received: *14 January, 1997;* revised: *1 June, 1998.*